A Comparison of Analysis and Forecast Correction Techniques: Impact of Negative Dissipation

CAROLYN A. REYNOLDS

Naval Research Laboratory, Monterey, California

(Manuscript received 5 July 1998, in final form 23 October 1998)

ABSTRACT

The impact of negative dissipation on posttime analysis and forecast correction techniques is examined in a simplified context. The experiments are conducted using a three-level quasigeostrophic model (with a nonsingular tangent propagator matrix) under a perfect-model assumption. Corrections to the initial analysis errors are obtained by operating on the forecast error with (i) the full inverse of the forward tangent propagator, (ii) an inverse composed of a subset of the first leading singular vectors (pseudoinverse), and (iii) the tangent equations with a negative time step (backward integration). When the forecast error is known exactly, using negative dissipation during the full-inverse or backward-integration calculation results in an analysis-error estimate that projects too weakly onto the leading singular vectors and too strongly onto the decaying singular vectors. These discrepancies are small for weak dissipation but increase as the dissipation strength is increased.

When the forecast error is known inexactly, negative dissipation provides a beneficial damping of the backward-in-time growth of uncertainties present in the forecast error. This damping effect is found to be due to a fairly uniform change in the singular values, not changes in the singular vectors. However, even for very strong negative dissipation, the uncertainty in the forecast error still grows during the full inverse or backward integration. Therefore, the analysis error estimate will still be dominated by the trailing singular vectors, which represent the decaying part of the initial error. This is in contrast to the pseudoinverse technique, which, like the adjoint sensitivity, is dominated by the fastest growing part of the initial error, and is therefore relatively insensitive to the analysis uncertainty contained within the forecast error. Thus, while full-inverse and backward-integration calculations may provide an analysis perturbation that results in a significantly improved forecast, the analysis error estimate is accurate only when the forecast error is known exactly (i.e., perfect model experiments), regardless of the sign of the dissipation. These results hold for both global and regional forecast errors.

1. Introduction

Given the demonstrated importance of accurate initial conditions for forecast skill (e.g., Rabier et al. 1996), as well as the importance of accurate reanalyses for atmospheric process studies, there has been much interest in techniques designed to diagnose analysis errors. Techniques for identifying the fastest growing part of the analysis error include adjoint and singular vector–based methods (Rabier et al. 1996; Buizza et al. 1997). Because these techniques focus on the growing part of the perturbation only, which at final time has a large signal-to-noise ratio, they are largely insensitive to the analysis uncertainty contained within the forecast error (Reynolds and Palmer 1998, hereafter RP98). This focus on the fastest growing part of the initial perturbation makes them well suited for adaptive observation purposes (Palmer et al. 1998), where the desired output is not an estimate of the full analysis error but rather the location of the portion of the analysis error that has the largest impact on the forecast.

In contrast, full-inverse and backward-integration (or quasi-inverse) techniques (Pu et al. 1997, 1998a,b; Wang et al. 1997; RP98) focus on the evolution of the entire perturbation, not just the growing portion. In perfect-model experiments, where the forecast error (actually, a forecast difference) is known exactly, the full inverse or the backward integration can provide a very good estimate of the full initial perturbation (as long as the forecast differences are only weakly nonlinear). However, RP98 shows that if true forecast errors are used, which can only be known inexactly, these techniques are susceptible to the rapid amplification of the final-time noise or uncertainty when going backward in time, owing to the erroneously large projection of the forecast error onto the decaying singular vectors (SVs). [The result that only the unstable component of the flow can be corrected through the assimilation of future data had been pointed out in variational studies such as Cohn

Corresponding author address: Dr. Carolyn A. Reynolds, 7 Grace Hopper Ave., Naval Research Laboratory, Monterey, CA 93943-5502.
E-mail: reynolds@nrlmry.navy.mil

et al. (1994) and Pires et al. (1996).] A mitigating factor when using full-inverse and backward-integration techniques is that the noise that grows when going backward in time then decays during the subsequent forward integration. This gives rise to the situation where the ''corrected'' analysis error is significantly further from the truth than the initial analysis error, yet produces a better forecast. This can occur even if the model is perfect.

Pu et al. (1998b) note different properties of adjoint and backward-integration techniques and propose a combination of these techniques for adaptive observation purposes. Pu et al. (1997) and Pu et al. (1998a,b) approximate the full inverse by running the tangent equations of the National Center for Environmental Prediction Medium-Range Forecast Model with a negative time step. They also change the sign of the dissipation terms during this backward integration in order to maintain computational stability. Wang et al. (1997) employ a similar technique in the context of data assimilation with a storm-scale model, pointing out that reversing the sign of the dissipation makes the dissipative, irreversible processes well posed in the backward integration. They likewise find that running the tangent linear equations with a negative time step and negative dissipation provides a reasonable approximation to the true inverse.

Using a simple model (with a nonsingular tangent propagator), the authors of RP98 were able to perform backward integrations with both positive and negative dissipation. Not surprisingly, they found that using negative instead of positive dissipation results in a worse approximation to the full inverse, and therefore gives a worse correction when the forecast errors are known exactly. A more interesting result was that when the forecast errors are known inexactly, the use of negative dissipation damps the backward growth of uncertainties, and thus is preferable to using positive dissipation in this case. However, the question of whether changing the sign of the dissipation significantly alters the characteristics of the analysis error estimate, particularly in regard to its growing and decaying properties, was not addressed. The application of a local projection operator during the backward integration was also not examined.

In this study, the impact of the sign of the dissipation on inverse-correction techniques in a perfect-model context is examined in detail. The forward tangent propagator is computed using both positive and negative dissipation terms (based on identical, positive dissipation, nonlinear trajectories). The differences between the associated positive- and negative-dissipation singular values and SVs are examined. The damping effect of the negative dissipation on the backward growth of uncertainty is of particular interest. The effects due to changes in the singular values and changes in the projection of the uncertainties onto the SVs are evaluated independently. Results are presented first for global error fields. Then, results based on a local projection operator are presented in order to assess implications for adaptive observations. True-inverse and backward-integration results are compared to pseudoinverse results. The linear theory, model description, and method outlined in sections 2, 3, and 4, respectively, are very similar to those described in RP98, although the nomenclature has changed slightly. Results are presented in section 5. A summary and conclusions are presented in section 6.

2. Linear theory

This study is done in the context of a ''perfect-model'' assumption. That is, one nonlinear trajectory is taken as ''truth,'' while another nonlinear trajectory, started from a different analysis that verifies at the same time, is taken as the ''forecast.'' In this situation the forecast ''error'' is due entirely to differences in the initial conditions. The analysis and forecast errors referred to in this study are actually analysis and forecast differences.

For a perfect model

$$\mathbf{L}\mathbf{e}_\mathbf{a} = \mathbf{e}_\mathbf{fl} = \mathbf{e}_\mathbf{f} - \mathbf{e}_\mathbf{fn}, \tag{1}$$

where $\mathbf{L}$ is the forward tangent propagator (tangent linear matrix) of the model, $\mathbf{e}_\mathbf{a}$ is the error at initial time and $\mathbf{e}_\mathbf{f}$ is the full nonlinear forecast error. The linear component of the forecast error is $\mathbf{e}_\mathbf{fl}$, while $\mathbf{e}_\mathbf{fn}$ is the difference between $\mathbf{e}_\mathbf{f}$ and $\mathbf{e}_\mathbf{fl}$ due to nonlinearities.

From (1), following Buizza et al. (1997) and Pu et al. (1997),

$$\mathbf{e}_\mathbf{a} \cong \mathbf{L}^{-1}\mathbf{e}_\mathbf{f}, \tag{2}$$

which indicates that if the inverse of the forward tangent propagator, or an approximation of it, is known, and the nonlinearities ($\mathbf{e}_\mathbf{fn}$) are very small, then operating on the forecast error with $\mathbf{L}^{-1}$ should approximate the analysis error.

Here $\mathbf{L}$ can be expressed in terms of singular vectors and singular values (see Molteni and Palmer 1993), such that

$$\mathbf{K}^{1/2}\mathbf{L}\mathbf{K}^{-1/2} = \mathbf{V}_\mathbf{K}\mathbf{\Sigma}_\mathbf{K}\mathbf{U}_\mathbf{K}^\mathrm{T}, \tag{3}$$

where $\mathbf{K}$ is a matrix to be defined below, $\mathbf{V}_\mathbf{K}$ is a matrix with columns that are the (left) SVs of $\mathbf{K}^{1/2}\mathbf{L}\mathbf{K}^{-1/2}$ at final time, $\mathbf{U}_\mathbf{K}$ is a matrix with columns that are the (right) SVs of $\mathbf{K}^{1/2}\mathbf{L}\mathbf{K}^{-1/2}$ at initial time, and $\mathbf{\Sigma}_\mathbf{K}$ is a diagonal matrix whose elements are the singular values of $\mathbf{K}^{1/2}\mathbf{L}\mathbf{K}^{-1/2}$, ranked in order of descending magnitude. Note that all matrices that are dependent upon the metric (norm) have the subscript $\mathbf{K}$. The first (last) column of $\mathbf{U}_\mathbf{K}$ represents the fastest growing (decaying) perturbation to the specific trajectory considered, which evolves into the first (last) column of $\mathbf{V}_\mathbf{K}$ and has an amplification factor given by the first (last) singular value.

The SVs and singular values depend on the metric $\mathbf{K}$. For studying forecast error growth, an appropriate metric should be based on analysis error covariances (Ehrendorfer and Tribbia 1997; Barkmeijer et al. 1998). However, given the uncertainties in current estimates of analysis error covariances, a kinetic energy metric is

used in this study. With this choice, $\mathbf{K}$ is a diagonal matrix such that for a state vector $\mathbf{x}$, $\mathbf{x}^T\mathbf{K}\mathbf{x}$ gives the kinetic energy (KE) of the system. The singular values (vectors) of $\mathbf{K}^{1/2}\mathbf{L}\mathbf{K}^{-1/2}$ are the KE singular values (vectors) of $\mathbf{L}$. The appropriateness of an energy-based metric for these applications is discussed in Palmer et al. (1998).

The inverse of the forward tangent propagator may be expressed in terms of the same singular values and SVs as above:

$$\mathbf{K}^{1/2}\mathbf{L}^{-1}\mathbf{K}^{-1/2} = \mathbf{U}_\mathbf{K}\mathbf{\Sigma}_\mathbf{K}^{-1}\mathbf{V}_\mathbf{K}^T. \quad (4)$$

A related quantity is the adjoint (transpose) tangent propagator, which can be expressed as

$$\mathbf{K}^{-1/2}\mathbf{L}^T\mathbf{K}^{1/2} = \mathbf{U}_\mathbf{K}\mathbf{\Sigma}_\mathbf{K}\mathbf{V}_\mathbf{K}^T. \quad (5)$$

Note from (4) and (5) how the inverse and the adjoint differ by the weighting of the singular values.

The full matrix $\mathbf{L}$ for even a relatively low-resolution adiabatic version of a forecast model is too large to represent explicitly and invert given current computing capabilities. However, Rabier et al. (1996) have used the adjoint equations operating on the forecast error to find the sensitivity of the forecast error to changes in the initial conditions, given by

$$\mathbf{s} = \mathbf{L}^T\mathbf{K}\mathbf{e}_\mathbf{f}. \quad (6)$$

Rabier et al. (1996) showed that a small analysis perturbation $\mathbf{a}_\mathbf{a} = \alpha\mathbf{K}^{-1}\mathbf{s}$, where α is an appropriate scaling factor, can significantly reduce errors in a nonlinear forecast. (Please note that in this study, ''adjoint-derived scaled sensitivity'' refers to a sensitivity perturbation that has been appropriately scaled by the metric, not to the sensitivity itself, which is actually a gradient, not a model state vector.) Buizza et al. (1997) have similarly been able to reduce the forecast error by using the pseudoinverse method. The pseudoinverse method uses $\mathbf{L}^{-1}$ as described in (4) but composed of only a limited subset of the fastest growing SVs in order to find the fastest growing components of $\mathbf{e}_\mathbf{a}$. The pseudoinverse $\mathbf{L}_{\mathbf{K},n}^{-1}$ is defined as

$$\mathbf{L}_{\mathbf{K},n}^{-1} = \mathbf{U}_{\mathbf{K},n}\mathbf{\Sigma}_{\mathbf{K},n}^{-1}\mathbf{V}_{\mathbf{K},n}^T. \quad (7)$$

where $\mathbf{U}_{\mathbf{K},n}$ ($\mathbf{V}_{\mathbf{K},n}$) is a rectangular matrix with columns composed of the first n initial-time (final-time) SVs of $\mathbf{K}^{1/2}\mathbf{L}\mathbf{K}^{-1/2}$ and $\mathbf{\Sigma}_{\mathbf{K},n}$ is a diagonal matrix composed of the first n singular values of $\mathbf{K}^{1/2}\mathbf{L}\mathbf{K}^{-1/2}$. The fastest growing part of the initial error can then be defined as

$$\mathbf{e}_\mathbf{a}^n = \mathbf{K}^{-1/2}\mathbf{L}_{\mathbf{K},n}^{-1}\mathbf{K}^{1/2}\mathbf{e}_\mathbf{f} \quad (8)$$

for small n. Note from (4) and (7) that when $n = 1449$, $\mathbf{L}_{\mathbf{K},n}^{-1} = \mathbf{K}^{1/2}\mathbf{L}^{-1}\mathbf{K}^{-1/2}$, which reduces (8) to $\mathbf{e}_\mathbf{a} = \mathbf{L}^{-1}\mathbf{e}_\mathbf{f}$. Thus, the calculation in (8) is not a function of the metric $\mathbf{K}$ when all of the SVs are included. For larger models, the first n SVs can be found through an iterative technique based on the Lanczos or Arnoldi algorithms and the tangent equations of the model. Gelaro et al. (1998) have shown $\mathbf{a}_\mathbf{a}$ and $\mathbf{e}_\mathbf{a}^n$ to have similar spatial patterns. The similarity of the spatial patterns of these fields is not surprising given that both $\mathbf{a}_\mathbf{a}$ and $\mathbf{e}_\mathbf{a}^n$ are dominated by the fastest growing SVs; $\mathbf{a}_\mathbf{a}$ because of the weighting of the singular values in the sensitivity in (5) and $\mathbf{e}_\mathbf{a}^n$ because only the fastest growing SVs are included in the calculation.

Pu et al. (1997) run the tangent equations with a negative time step (and negative dissipation) starting with the forecast error to approximate $\mathbf{L}^{-1}\mathbf{e}_\mathbf{f}$, and produce an estimate of the full analysis error. They find that this technique yields forecast corrections as good as those using five iterations of the adjoint (Rabier et al. 1996). They also find that this technique yields good estimates of the analysis error in perfect-model experiments where the forecast error is known exactly.

3. Model description

The model used in this study is the quasigeostrophic potential vorticity (PV) model described in Marshall and Molteni (1993). The model is run with a T21 truncation and has three levels corresponding to 800, 500, and 200 mb. The state vector has 1449 nonzero components, and therefore is small enough so that $\mathbf{L}$ can be calculated and inverted explicitly. As will be shown, the condition number of $\mathbf{L}$ is relatively small, so that the inversion is accurate. The model forcing is composed of spatially varying source terms of PV that correspond to a northern winter climatology. The model has three types of dissipative forcing. For the control case, the dissipative terms are Newtonian relaxation of temperature between levels with a relaxation coefficient of 25 day^{-1}, an 800-mb linear drag term that varies with topography from 3 to 1.5 day^{-1}, and horizontal scale-selective (∇^8) dissipation operating on the PV such that spherical harmonics of the time-varying PV with a total wavenumber of 21 are damped on a 2-day timescale. For ''strong'' dissipation, all the dissipation timescales are reduced by 50%. For ''medium'' dissipation, the timescales are reduced by 25%.

The model has been used in several previous studies involving SVs [e.g., for finite-time instability by Molteni and Palmer (1993), for ensemble prediction by Mureau et al. (1993), for skill prediction methods by Barkmeijer et al. (1993)]. The model is well suited for these types of studies, since it is complex enough to capture baroclinic synoptic-scale processes important in forecast error growth, but is small enough so that $\mathbf{L}$ can be calculated and inverted explicitly.

4. Method

The matrix $\mathbf{L}$ is constructed by running the tangent equations 1449 times as described in RP98. The matrix $\mathbf{R}$ is calculated in a similar fashion to $\mathbf{L}$, but with negative instead of positive-dissipation terms in the tangent equations. However, $\mathbf{R}$ and $\mathbf{L}$ are based on identical nonlinear orbits with positive dissipation. Numerical al-

gorithm routines are used to calculate both the inverse and the KE singular values and vectors of $\mathbf{L}$ and $\mathbf{R}$. The KE singular values and initial-time and final-time SVs of $\mathbf{L}$ are referred to as σ_i^+, $\mathbf{u}_i^+$, and $\mathbf{v}_i^+$, respectively. Likewise, the KE singular values and SVs of $\mathbf{R}$ are referred to as σ_i^-, $\mathbf{u}_i^-$, and $\mathbf{v}_i^-$. All results shown in this paper correspond to an integration time of 48 h, and a kinetic energy metric. In the first part of this study, the differences between the KE singular values and SVs for $\mathbf{L}$ and $\mathbf{R}$ are examined.

The second part of this study concerns the impact of the sign of the dissipation on the posttime forecast and analysis correction techniques as described in RP98 and summarized here. Two 48-h nonlinear integrations of the quasigeostrophic model are performed using different European Centre for Medium-Range Weather Forecasts analyses for the same date. The integration starting from the 3D variational (3DVAR) analysis (Andersson et al. 1995), referred to as $\mathbf{f}_{3\mathrm{DVAR}}$ is taken as the truth, while a 48-h nonlinear integration starting from the optimal interpolation (OI) analysis for the same time, $\mathbf{f}_{\mathrm{OI}}$, is taken as the forecast. The exact forecast error is defined as

$$\mathbf{e}_\mathbf{f} = \mathbf{f}_{\mathrm{OI}} - \mathbf{f}_{3\mathrm{DVAR}}. \tag{9}$$

The forecast error is operated on with $\mathbf{L}^{-1}$ based on the OI 48-h trajectory to get an estimate of the analysis error $\mathbf{e}_{\mathbf{a}1}$, that is

$$\mathbf{e}_{\mathbf{a}1} = \mathbf{L}^{-1}\mathbf{e}_\mathbf{f}. \tag{10}$$

Then, $\mathbf{e}_{\mathbf{a}1}$ is subtracted from the OI analysis to produce a corrected analysis and a third nonlinear integration, referred to as $\mathbf{f}_1$, is run from these initial conditions. The corrected forecast error is then given by

$$\mathbf{e}_{\mathbf{f}1} = \mathbf{f}_1 - \mathbf{f}_{3\mathrm{DVAR}}. \tag{11}$$

To simulate the more realistic case where the forecast error is not known exactly, uncertainty, $\boldsymbol{\delta}$, is added to the forecast error, $\mathbf{e}_\mathbf{f}$, before being operated on with $\mathbf{L}^{-1}$, such that

$$\mathbf{e}_{\mathbf{a}2} = \mathbf{L}^{-1}(\mathbf{e}_\mathbf{f} + \boldsymbol{\delta}), \tag{12}$$

where $\boldsymbol{\delta}$ is equal to the difference between the 3DVAR analysis and the OI analysis valid 48 h after the start of the integration time. Thus, $\boldsymbol{\delta}$ represents the uncertainty in the forecast error due to uncertainty in the final-time analysis. It is approximately the same magnitude as the analysis error 48 h earlier. The final step is to perform a fourth nonlinear integration with the initial conditions based on the OI analysis minus $\mathbf{e}_{\mathbf{a}2}$ yielding the second corrected forecast $\mathbf{f}_2$, such that

$$\mathbf{e}_{\mathbf{f}2} = \mathbf{f}_2 - \mathbf{f}_{3\mathrm{DVAR}}. \tag{13}$$

Thus, the initial analysis error estimates and corrected forecast errors with the subscript 1 are based on the unrealistic case where the forecast error is known exactly. The initial analysis error estimates and corrected forecast errors with the subscript 2 are based on the more realistic case where the forecast error is not known exactly. Throughout this study, $\mathbf{e}_\mathbf{f}$ is referred to as the *exact* forecast error, and $\mathbf{e}_\mathbf{f} + \boldsymbol{\delta}$ is referred to as the *inexact* forecast error.

Both sets of experiments described above are also performed using the tangent equations with a negative time step in place of using the actual $\mathbf{L}^{-1}$, as described in RP98. This is done with both positive- and negative-dissipation terms. The analysis error estimates and the corrected forecast errors from these backward integrations will be referred to as $\mathbf{e}_{\mathbf{a}1}^{+B}$, $\mathbf{e}_{\mathbf{a}2}^{+B}$, $\mathbf{e}_{\mathbf{f}1}^{+B}$, and $\mathbf{e}_{\mathbf{f}2}^{+B}$ when positive dissipation is used, and $\mathbf{e}_{\mathbf{a}1}^{-B}$, $\mathbf{e}_{\mathbf{a}2}^{-B}$, $\mathbf{e}_{\mathbf{f}1}^{-B}$, and $\mathbf{e}_{\mathbf{f}2}^{-B}$ when negative dissipation is used.

Both sets of perfect-model experiments are also repeated using the pseudoinverse method (Buizza et al. 1997; RP98). That is, the analysis error estimates are defined as $\mathbf{e}_{\mathbf{a}1}^{+n} = \mathbf{K}^{-1/2}\mathbf{L}_{\mathbf{K},n}^{-1}\mathbf{K}^{1/2}(\mathbf{e}_\mathbf{f})$ and $\mathbf{e}_{\mathbf{a}2}^{+n} = \mathbf{K}^{-1/2}\mathbf{L}_{\mathbf{K},n}^{-1}\mathbf{K}^{1/2}(\mathbf{e}_\mathbf{f} + \boldsymbol{\delta})$. The subsequent corrected forecast errors for these experiments will be referred to as $\mathbf{e}_{\mathbf{f}1}^{+n}$ and $\mathbf{e}_{\mathbf{f}2}^{+n}$. When $n = 1449$, the pseudoinverse equals the true inverse, and the superscript n is dropped. Similar pseudoinverse experiments are performed using the negative-dissipation SVs and singular values; that is, the analysis error estimates are defined as $\mathbf{e}_{\mathbf{a}1}^{-n} = \mathbf{K}^{-1/2}\mathbf{R}_{\mathbf{K},n}^{-1}\mathbf{K}^{1/2}(\mathbf{e}_\mathbf{f})$ and $\mathbf{e}_{\mathbf{a}2}^{-n} = \mathbf{K}^{-1/2}\mathbf{R}_{\mathbf{K},n}^{-1}\mathbf{K}^{1/2}(\mathbf{e}_\mathbf{f} + \boldsymbol{\delta})$. The subsequent corrected forecast errors for these experiments will be referred to as $\mathbf{e}_{\mathbf{f}1}^{-n}$ and $\mathbf{e}_{\mathbf{f}2}^{-n}$.

The terms used in the paper are summarized here. The pseudoinverse is the inverse of the forward tangent propagator composed of a subset of the leading SVs and singular values. When all the SVs and singular values are included, then this is called the full inverse. If using the positive-dissipation SVs and singular values, then this full inverse is the true inverse. The backward-integration technique (which is an approximation to the full inverse) refers to running the tangent equations with a negative time step and using either positive or negative dissipation. Refer to Table 1 for a summary of the nomenclature.

5. Results

a. Dependence of singular values and vectors on dissipation

In RP98 it was found that the backward-integration technique (with positive dissipation) is a very close approximation to the true inverse ($\mathbf{L}^{-1}$). A similar comparison is made here between the backward integration technique with negative dissipation and $\mathbf{R}^{-1}$. Table 2 shows the percent difference between the full inverse and backward integration operating on the inexact forecast error for the different dissipation strengths and signs. The differences between the positive-dissipation full inverse and the positive-dissipation backward integration (column 1) and the negative-dissipation full inverse and the negative-dissipation backward integration (column 2) range between 5% and 11%. This in-

TABLE 1. Explanation of nomenclature. The first subscript on **e** is **a** for an analysis error estimate or **f** for a corrected forecast error. The second subscript is 1 if the estimate/correction is based on the exact forecast error, or 2 if the estimate/correction is based on the inexact forecast error. The first superscript ± indicates the sign of the dissipation in the method. The second superscript is *B* if the backward integration technique is employed or *n* where *n* indicates the number of SVs included in the pseudoinverse. If all the SVs are included (i.e., $n = 1449$, the full inverse is used) the second subscript is dropped.

Analysis error estimate	Corrected forecast error	Method	Forecast error	Sign of dissipation
$\mathbf{e}_{\mathbf{a}1}^{+(n)}$	$\mathbf{e}_{\mathbf{f}1}^{+(n)}$	Inverse (psuedoinverse if $n < 1449$)	Exact	Positive
$\mathbf{e}_{\mathbf{a}2}^{+(n)}$	$\mathbf{e}_{\mathbf{f}2}^{+(n)}$	Inverse (psuedoinverse if $n < 1449$)	Inexact	Positive
$\mathbf{e}_{\mathbf{a}1}^{-(n)}$	$\mathbf{e}_{\mathbf{f}1}^{-(n)}$	Inverse (psuedoinverse if $n < 1449$)	Exact	Negative
$\mathbf{e}_{\mathbf{a}2}^{-(n)}$	$\mathbf{e}_{\mathbf{f}2}^{-(n)}$	Inverse (psuedoinverse if $n < 1449$)	Inexact	Negative
$\mathbf{e}_{\mathbf{a}1}^{+B}$	$\mathbf{e}_{\mathbf{f}1}^{+B}$	Backward integration	Exact	Positive
$\mathbf{e}_{\mathbf{a}2}^{+B}$	$\mathbf{e}_{\mathbf{f}2}^{+B}$	Backward integration	Inexact	Positive
$\mathbf{e}_{\mathbf{a}1}^{-B}$	$\mathbf{e}_{\mathbf{f}1}^{-B}$	Backward integration	Exact	Negative
$\mathbf{e}_{\mathbf{a}2}^{-B}$	$\mathbf{e}_{\mathbf{f}2}^{-B}$	Backward integration	Inexact	Negative

TABLE 2. Percent difference between the full inverse operating on the inexact forecast error and the backward integration of the inexact forecast error.

	Positive inverse vs positive backward integration	Negative inverse vs negative backward integration	Positive inverse vs negative backward integration
Control dissipation	11%	11%	17%
Medium dissipation	7%	8%	26%
Strong dissipation	5%	7%	37%

dicates that the backward integration is a good approximation to the full inverse in both positive- and negative-dissipation cases. As expected, the percent differences between the positive-dissipation full inverse (the true inverse) and the negative-dissipation backward integration (similar to that used in practice at NCEP) are larger, ranging from 17% for control dissipation to 37% for strong dissipation. (The reader is reminded that the sign of the dissipation is altered only during the tangent propagator calculations. The sign of the dissipation in the nonlinear orbit integration is always positive). This indicates that the negative-dissipation backward integration is a reasonable approximation to the true inverse. However, the approximation becomes worse as the magnitude of the dissipation becomes larger.

Since the negative-dissipation backward integration is indeed similar to $\mathbf{R}^{-1}$, the impact of the sign of the dissipation on the backward integration can be examined in terms of the negative-dissipation singular values and vectors. Figure 1 shows the natural log of the positive- and negative-dissipation KE singular values divided by 2 [$\ln(\boldsymbol{\sigma}_i^+)/2$ and $\ln(\boldsymbol{\sigma}_i^-)/2$, which is the inverse of the *e*-folding time in days]. For the control dissipation case (Fig. 1a), approximately 625 of the positive-dissipation SVs are growing [i.e., $\ln(\boldsymbol{\sigma}_i^+)/2 > 0.0$ for $i < 625$]. When the sign of the dissipation is reversed (dashed line), then all of the singular values become larger (i.e., $\boldsymbol{\sigma}_i^- > \boldsymbol{\sigma}_i^+$), and the growing subspace expands to include approximately 875 SVs. The negative-dissipation singular values are actually very similar to the singular values of $\mathbf{L}^{-1}$, shown in RP98. As the strength of the dissipation is increased (Fig. 1b), all of the positive-dissipation singular values become smaller [consistent with the results of Buizza (1998)]. Likewise, all of the negative-dissipation singular values become larger.

It should be noted that all the singular values are nonzero, and therefore $\mathbf{L}$ is invertible. The condition number (ratio of largest to smallest singular value) of $\mathbf{L}$ gives an indication of the accuracy at which $\mathbf{L}$ can be inverted. For control dissipation, $\boldsymbol{\sigma}_1^+/\boldsymbol{\sigma}_{1449}^+ = 9.29/0.088$ and $\boldsymbol{\sigma}_1^-/\boldsymbol{\sigma}_{1449}^- = 14.17/0.123$, giving condition numbers of approximately 106 and 115. For strong dissipation, $\boldsymbol{\sigma}_1^+/\boldsymbol{\sigma}_{1449}^+ = 5.66/0.075$ and $\boldsymbol{\sigma}_1^-/\boldsymbol{\sigma}_{1449}^- = 13.85/0.189$, giving condition numbers of approximately 75 and 73. These relatively low condition numbers indicate that $\mathbf{L}$ can be inverted accurately. Tests involving the tangent linear equations and $\mathbf{L}^{-1}$ composed of the SVs and singular values confirm this.

The difference between the positive- and negative-dissipation singular values becomes larger as the strength of the dissipation is increased. The average ratio of the negative-dissipation singular values to the positive-dissipation singular values ($\boldsymbol{\sigma}_i^-/\boldsymbol{\sigma}_i^+$) is 1.49 for control dissipation and 2.40 for strong dissipation. (The ratios for squared streamfunction singular values, not shown, are 1.49 and 2.24.) This ratio remains approximately constant for all *i* for control dissipation. For strong dissipation, the ratio is smaller for the near-neutral singular values, but is approximately the same for the majority of the growing and decaying singular values. If the positive- and negative-dissipation SVs are the same, or very similar, the impact of changing the sign of the dissipation would be similar to multiplying the field by a constant (e.g., $\mathbf{Re} = 1.49\,\mathbf{Le}$ and $\mathbf{R}^{-1}\mathbf{e} = \mathbf{L}^{-1}\mathbf{e}/1.49$ for the control dissipation case), rather than changing the spatial structure of the field. If $\boldsymbol{\sigma}_i^-/\boldsymbol{\sigma}_i^+$ exhibited a significant trend with rank, then changing the sign of the dissipation would have affected the structure, as well as the magnitude, of the result.

The singular values are directly related to perturbation variance growth. The linear growth of the variance of an initial perturbation that is isotropic with respect to the initial-time SVs is given by the mean square of the singular values (Lorenz 1965; Farrell 1990). Likewise, the backward-in-time growth of a perturbation that is isotropic with respect to the final-time SVs is given by the mean square of the inverse of the singular values. Although the analysis differences examined here are not strictly isotropic, these calculations can act as an ap-

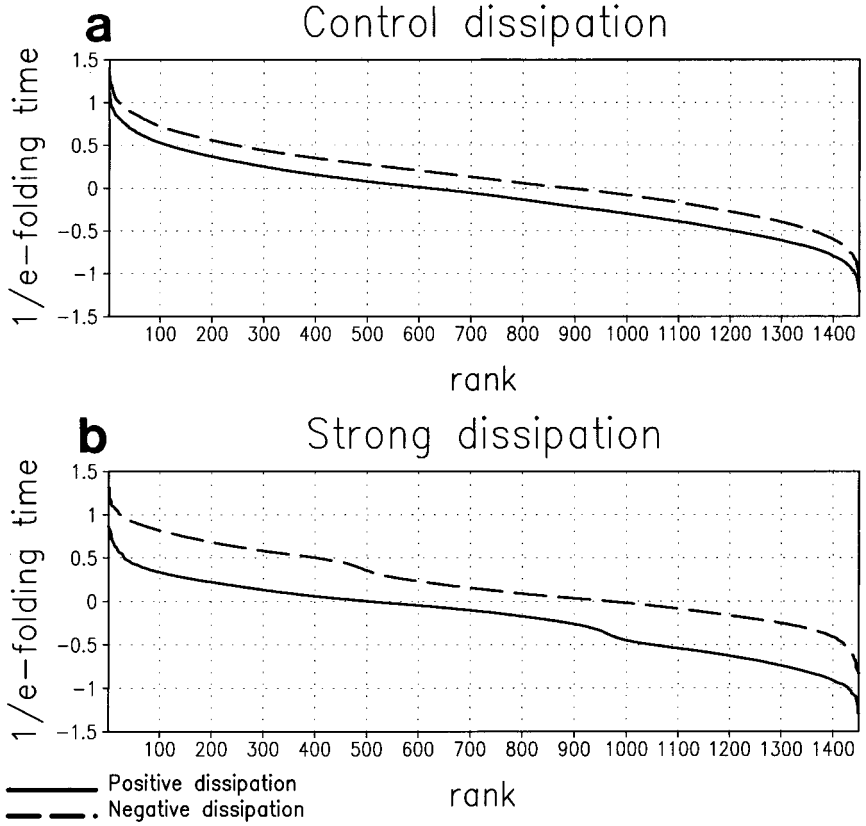

FIG. 1. The natural log of the KE singular values divided by 2 (the inverse of the *e*-folding time) for (a) control dissipation and (b) strong dissipation for positive (solid) and negative (dashed) dissipation. Units are day^{-1}.

proximation for the relative forward and backward growth of uncertainty.

The positive- and negative-dissipation mean-square singular values are given in Table 3. As pointed out in RP98, for (positive) dissipative systems, the backward-in-time growth of an isotropic perturbation will be larger than the forward-in-time growth. This inequality becomes greater as the strength of the dissipation is increased. For negative dissipation, the backward growth of uncertainty is smaller than the forward growth of uncertainty. The backward-in-time growth of this uncertainty will be much smaller when using negative dissipation than when using positive dissipation. This is consistent with the apparent damping effect of the negative dissipation on the backward growth of analysis uncertainty found in RP98. It is important to note, however, that even for the strong negative-dissipation case, the backward growth of an isotropic perturbation would still be positive (i.e., the uncertainty present at final time will grow during the inverse calculation, not decay).

TABLE 3. Linear growth of variance of a perturbation that is isotropic with respect to the SVs.

	$\frac{1}{1449}\sum_{i=1}^{1449}\sigma_i^2$	$\frac{1}{1449}\sum_{i=1}^{1449}\sigma_i^{-2}$
Control positive	2.5	4.6
Medium positive	1.8	5.6
Strong positive	1.3	7.2
Control negative	5.6	2.1
Medium negative	6.2	1.6
Strong negative	7.3	1.2

As stated above, if the SVs are relatively immune to changes in the sign of the dissipation, then Fig. 1 indicates that the impact of this change would be similar to multiplying the field by a constant. Buizza (1998) has shown that changing the strength of the horizontal diffusion can have a significant impact on the structures of the leading SVs. [For a discussion of the structures of the leading and trailing SVs in this model, see Molteni and Palmer (1993) and RP98.] The results of the current study also show that changing the sign of the dissipation alters the SVs. Figure 2a shows the percent variance of the first five positive-dissipation SVs that can be explained by negative-dissipation SVs 1 through *n* (where *n* varies from 1 to 30). Likewise, Fig. 2b shows the percent variance of the last five positive-dissipation SVs that can be explained by negative-dissipation SVs *n* through 1449 (where *n* varies from 1420 to 1449). Two trends are apparent. First, the similarities between the

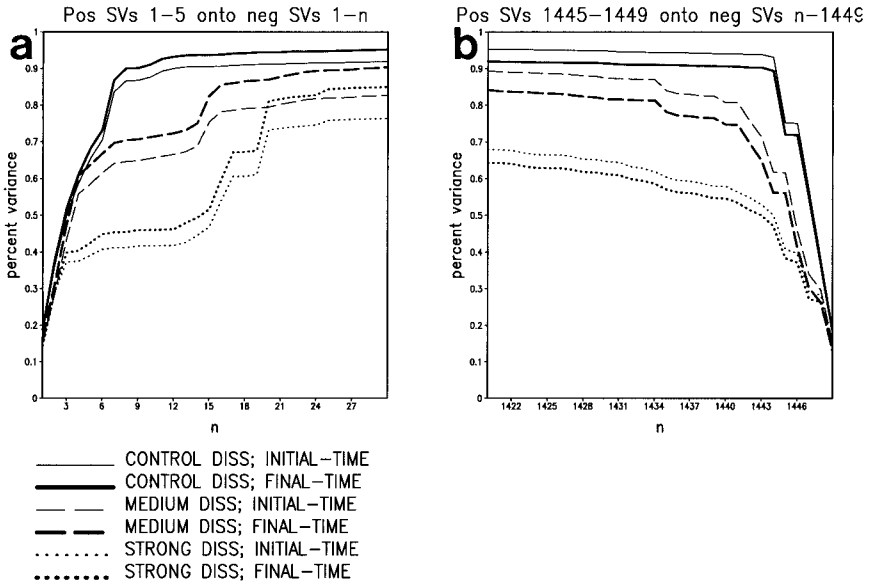

FIG. 2. The percent variance of (a) the first five positive-dissipation SVs explained by the first n negative-dissipation SVs and (b) the last five positive-dissipation SVs explained by the last n negative-dissipation SVs. The percent variance is measured in terms of kinetic energy. Control, medium, and strong dissipation results are indicated by the solid, dashed, and dotted curves, respectively. The initial- (final-) time SVs are indicated by the thin (thick) curves.

positive- and negative-dissipation SVs decrease as the magnitude of the dissipation is increased. Second, the leading SVs are somewhat less sensitive to the sign of the dissipation than the trailing SVs. These trends are also apparent when examining the first and last 30, or first and last 100 SVs. This implies that the accuracy of a negative-dissipation backward integration will be a function of the strength of the dissipation.

Since the positive- and negative-dissipation SVs are not identical (Fig. 2), the projection of the forecast error or analysis error onto the negative-dissipation SVs will differ from the projection onto the positive-dissipation SVs. An important question to ask is whether these differences are small and random in nature, or systematic. If there is a significant trend with rank in the difference, then the character of the estimated analysis error may change significantly with a change in the sign of the dissipation. For example, if the analysis uncertainty at final time ($\boldsymbol{\delta}$) has a smaller projection onto the trailing $\mathbf{v}_i^-$ than onto the trailing $\mathbf{v}_i^+$, then the problem of the backward growth of uncertainties might be considerably mitigated when using negative dissipation. However, if the projection of $\mathbf{e_f}$ onto $\mathbf{v}_i^-$ is substantially different from the projection onto $\mathbf{v}_i^+$, then the estimate of the initial analysis error might be significantly degraded.

To investigate these possibilities, the magnitudes of the projections of analysis error and exact and inexact forecast error onto positive- and negative-dissipation SVs are shown in Figs. 3–5. All curves shown in Figs. 3–5 have been smoothed using a 35-item running mean. Figure 3a shows the magnitude of the projection of analysis error onto the initial-time SVs ($\mathbf{e_a}; \mathbf{u}_i^+$), denoted by the dotted line [where (. . . ; . . .) indicates a KE inner product]. As shown in RP98, although noisy, the curve does not show a strong trend with rank. The projection of the exact forecast error onto the positive-dissipation final-time SVs ($\mathbf{e_f}; \mathbf{v}_i^+$) is denoted by the thick solid line. The error growth here is approximately linear [i.e., ($\mathbf{e_f}; \mathbf{v}_i^+$) $\cong \sigma_i(\mathbf{e_a}; \mathbf{u}_i^+)$], so that for the growing SVs ($\mathbf{e_f}; \mathbf{v}_i^+$) $>$ ($\mathbf{e_a}; \mathbf{u}_i^+$), while for the decaying SVs ($\mathbf{e_f}; \mathbf{v}_i^+$) $<$ ($\mathbf{e_a}; \mathbf{u}_i^+$). The projection of the forecast error onto the negative-dissipation final-time SVs ($\mathbf{e_f}; \mathbf{v}_i^-$) is also shown in Fig. 3a (thin solid line). Note that ($\mathbf{e_f}; \mathbf{v}_i^+$) and ($\mathbf{e_f}; \mathbf{v}_i^-$) are very similar, although ($\mathbf{e_f}; \mathbf{v}_i^-$) is larger than ($\mathbf{e_f}; \mathbf{v}_i^+$) for the trailing SVs. For strong dissipation (Fig. 3b), the differences between negative and positive dissipation become more apparent. In this case, ($\mathbf{e_f}; \mathbf{v}_i^-$) is two or three times as large as ($\mathbf{e_f}; \mathbf{v}_i^+$) for the trailing SVs. At the same time, ($\mathbf{e_f}; \mathbf{v}_i^-$) is significantly smaller than ($\mathbf{e_f}; \mathbf{v}_i^+$) for the leading SVs. This should result in an analysis error estimate that projects too strongly onto the decaying modes relative to the growing modes. This suggests that the negative-dissipation inverse becomes less accurate as the strength of the dissipation increases, consistent with the results shown in Table 2.

As shown in RP98, the problem with full-inverse and backward-integration methods occurs when uncertainty is introduced into the forecast error. This uncertainty has a significant projection onto the trailing final-time SVs, which grow when going backward. The projections of the analysis uncertainty onto the positive and negative control dissipation final-time SVs, ($\boldsymbol{\delta}; \mathbf{v}_i^+$) and ($\boldsymbol{\delta}; \mathbf{v}_i^-$), are shown in Fig. 4. The projection of the analysis un-

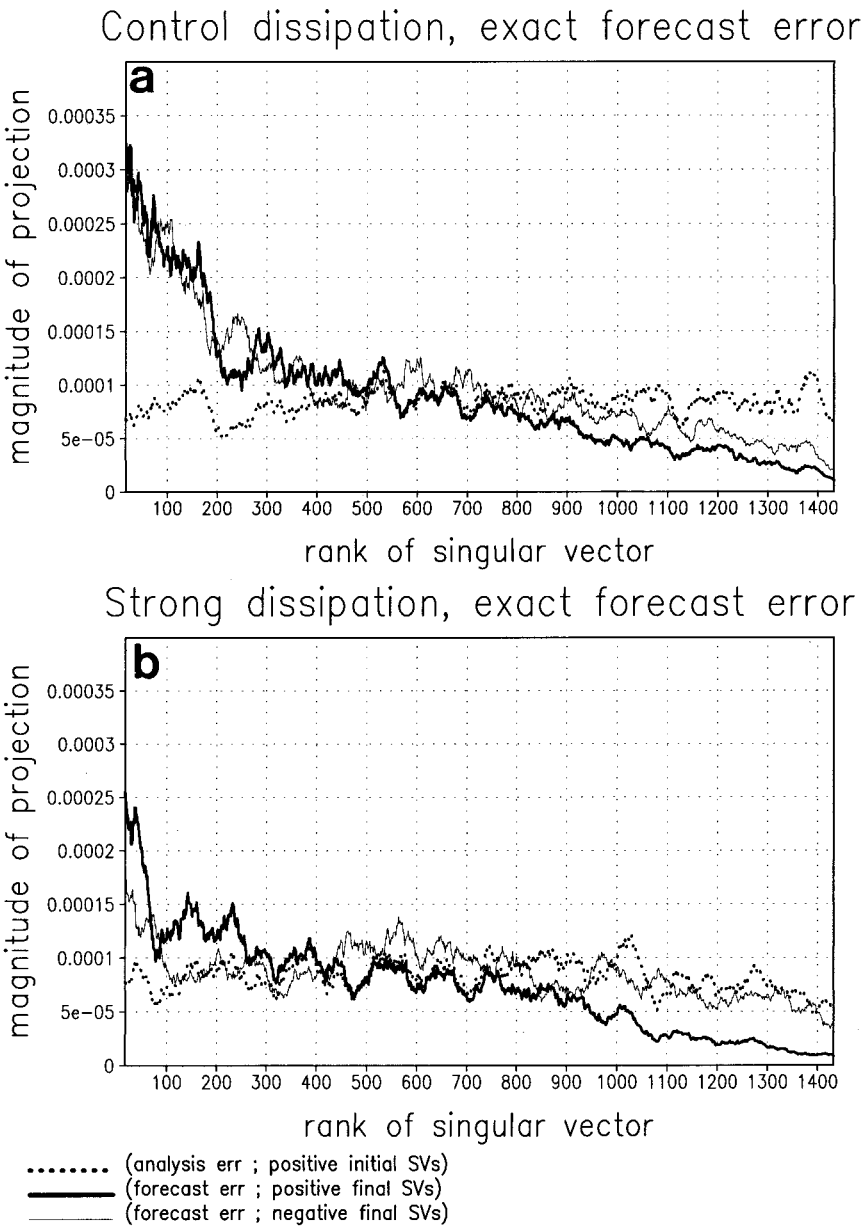

FIG. 3. The magnitude of the projection of the initial analysis error onto the initial-time positive-dissipation SVs (dotted), exact forecast error onto the final-time positive-dissipation SVs (thick solid), and the exact forecast error onto the final-time negative-dissipation SVs (thin solid), as a function of rank. (a) Control dissipation case and (b) strong dissipation case.

certainty onto the negative-dissipation trailing SVs is at least as large as the projection onto the positive-dissipation trailing SVs. The results for strong dissipation (not shown) are similar. The amplification of this noise during the inverse calculation should occur in both cases, although the magnitude of the amplification, determined by the singular values, will differ.

The projections of the inexact forecast error onto the final-time SVs, $(\mathbf{e_f} + \boldsymbol{\delta}; \mathbf{v}_i^+)$ and $(\mathbf{e_f} + \boldsymbol{\delta}; \mathbf{v}_i^-)$, are shown in Fig. 5 for control dissipation. The projection of the forecast error onto the leading positive-dissipation SVs is relatively insensitive to the addition of uncertainty. However, the projection onto the trailing SVs increases significantly with the inclusion of uncertainty in the forecast error (cf. Fig. 5 with Fig. 3a). It is this erroneous projection of the noise onto the decaying SVs that causes problems when using full-inverse or backward-integration techniques. These figures indicate that this erroneous projection is not mitigated by using negative dissipation, suggesting that the damping effect of negative dissipation on the backward growth of uncertainty is due to changes in the singular values, not changes in

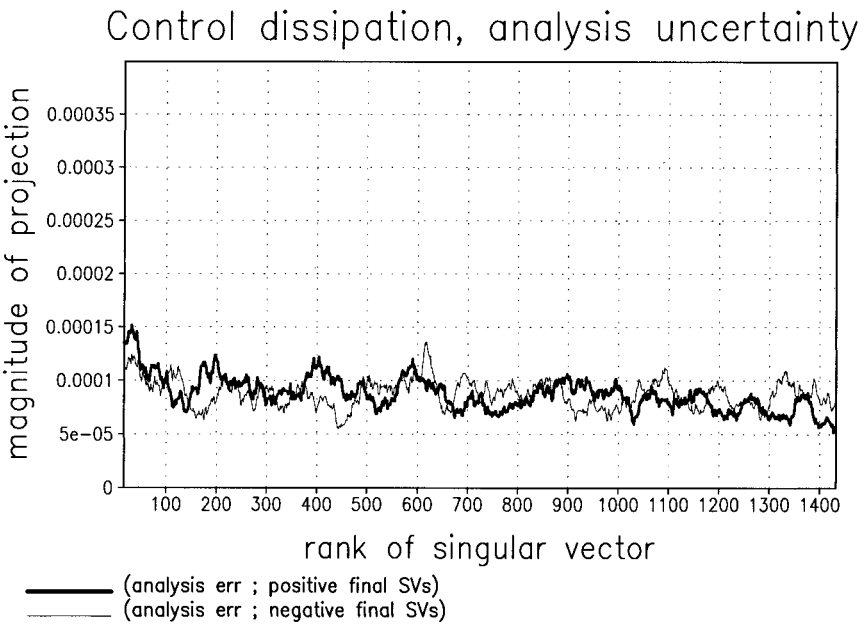

FIG. 4. The magnitude of the projection of the analysis uncertainty $\boldsymbol{\delta}$ onto the positive-dissipation final-time SVs (thick solid) and negative-dissipation final-time SVs (thin solid) for control dissipation.

the SVs. Results based on squared streamfunction SVs (not shown) lead to similar conclusions.

b. Global correction methods

To confirm the relative impact of the SVs and singular values suggested in the preceding subsection, full-inverse corrections are applied by mixing and matching the positive (negative) singular values with the positive (negative) SVs. The best analysis and forecast corrections based on exact forecast errors are obtained by using both positive-dissipation SVs and singular values, as expected, with the other combinations slightly less optimal.

Corrected analysis and forecast errors based on the inexact forecast error are shown in Tables 4 and 5 (in terms of globally averaged mean square geopotential height). Using both positive-dissipation SVs and singular values gives a corrected analysis error of 381 m^2 (up from the uncorrected analysis error of 130 m^2). If negative-dissipation singular values are used instead of the positive-dissipation singular values, then the corrected analysis error improves to 195 m^2 (still worse than the uncorrected analysis error). If negative-dissipation SVs are used instead of the positive-dissipation SVs, then the corrected analysis error becomes far worse (510 m^2). Clearly, the beneficial impact is coming from the negative-dissipation singular values, not the SVs. Similar results are found when considering the corrected forecast error (Table 5). Even though the corrected analysis errors are worse than the uncorrected analysis error (Table 4), the corrected forecast errors are better than the uncorrected forecast error (Table 5). In fact, the corrected analysis errors are actually larger than the corrected forecast errors, indicating that the initial perturbation actually shrinks with time.

To compare the impact of uncertainty in the different correction methods, the positive- and negative-dissipation pseudoinverse corrected analysis errors are shown in Fig. 6a and corrected forecast errors are shown in Fig. 6b. When the forecast errors are known exactly (thick lines), it is always best to use positive dissipation. When uncertainty is added to the forecast error (thin lines), negative dissipation is preferable when using the full inverse (pseudoinverse with $n = 1449$), but positive dissipation is preferable for a pseudoinverse composed of only the first few SVs (small n). This is because the pseudoinverse for small n is relatively insensitive to analysis uncertainty contained within the forecast error.

It is instructive to look at the spatial patterns associated with the different techniques to examine the structural differences in the analysis error estimates. Figure 7 shows the Northern Hemisphere 500-mb geopotential height field for the initial analysis error ($\mathbf{e}_\mathbf{a}$, Fig. 7a) and the associated exact forecast error ($\mathbf{e}_\mathbf{f}$, Fig. 7b). The estimate of the initial analysis error and the associated corrected forecast error when using the true inverse ($\mathbf{e}_{\mathbf{a}1}^{+}$ and $\mathbf{e}_{\mathbf{f}1}^{+}$), and the backward integration with negative dissipation ($\mathbf{e}_{\mathbf{a}1}^{-B}$ and $\mathbf{e}_{\mathbf{f}1}^{-B}$) are also shown. In this case, when the forecast error is known exactly, both techniques provide a very good estimate of the analysis error (Figs. 7c and 7e). The true inverse mean square corrected analysis error ($\mathbf{e}_\mathbf{a} - \mathbf{e}_{\mathbf{a}1}^{+}$) is only 8 m^2, illustrating the small effect of nonlinearities in this case. The neg-

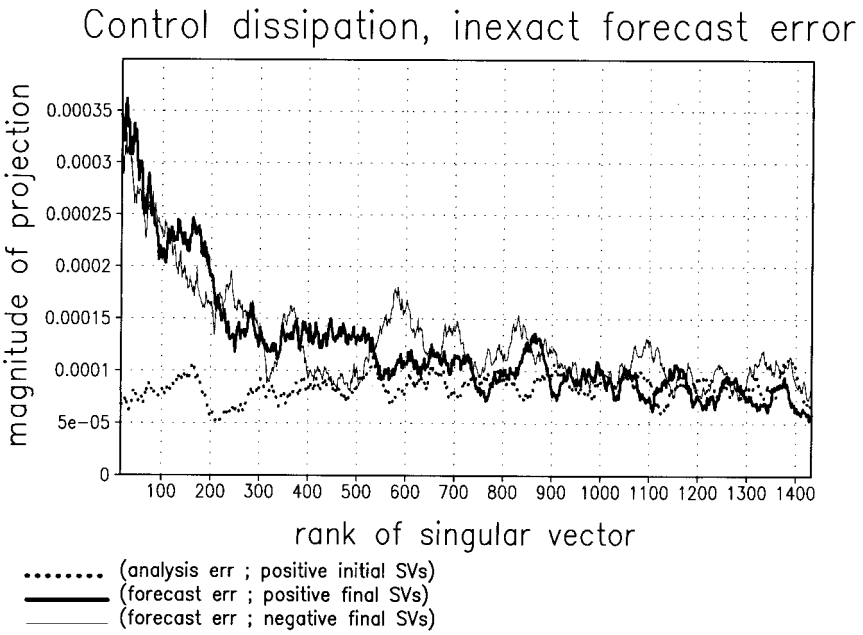

FIG. 5. Same as Fig. 3a except for inexact forecast error ($\mathbf{e}_f + \boldsymbol{\delta}$) instead of exact forecast error.

ative-dissipation backward-integration corrected analysis error ($\mathbf{e}_a - \mathbf{e}_{a1}^{-B}$) is only 23 m^2, much smaller than the uncorrected analysis error of 130 m^2. The subsequent corrected forecasts (Figs. 7d,f) have even smaller mean square errors (5 m^2 for the true inverse and 19 m^2 for the negative-dissipation backward integration, compared with 245 m^2 for the uncorrected forecast error). Consistent with the results of RP98, this shows that the negative-dissipation backward integration gives corrections that are almost as good as those obtained using the true inverse when forecast errors are known exactly.

Figure 8 shows the analogous analysis error estimates and the corrected forecast errors based on the inexact forecast error (i.e., $\mathbf{e}_{a2}^{+}$, $\mathbf{e}_{f2}^{+}$, and $\mathbf{e}_{a2}^{-\mathbf{B}}$, $\mathbf{e}_{f2}^{-\mathbf{B}}$). Now both analysis error estimates ($\mathbf{e}_{a2}^{+}$ and $\mathbf{e}_{a2}^{-\mathbf{B}}$, shown in Figs. 8a,c, respectively) have magnitudes that are far too large, particularly for the true-inverse case, and neither estimate looks much like the true analysis error shown in Fig. 7a. In fact, the corrected analysis errors of 381 m^2 and 261 m^2 are much larger than the 130 m^2 of the uncorrected analysis error. These estimates are dominated by the backward-in-time amplification of $\boldsymbol{\delta}$ (not shown). Also note that the patterns in Figs. 8a and 8c are very similar, indicating that the change in the sign of the dissipation is primarily changing the magnitude of the field, rather than the structure. The resulting forecast errors ($\mathbf{e}_{f2}^{+}$ and $\mathbf{e}_{f2}^{-\mathbf{B}}$, shown in Figs. 8b,d, respectively) of 148 m^2 and 123 m^2 are larger than those found for the exact forecast error (Figs. 7d,f), but nevertheless are a significant improvement over the uncorrected forecast error of 245 m^2 (Fig. 7b). The results shown in Fig. 8 illustrate that even very large analysis errors can result in relatively small forecast errors (within the linear regime), given that these errors project strongly onto the decaying SVs. In fact, these analysis errors are actually larger than the forecast errors. It is entirely possible to find a ''corrected'' analysis that has a significantly larger error than the uncorrected analysis, yet results in a better forecast.

The difference between using the true inverse and the negative-dissipation backward integration are more clearly illustrated by the strong-dissipation results. Fig-

TABLE 4. Corrected analysis error (m^2) based on the inexact forecast error using the full inverse composed of positive- or negative-dissipation SVs and singular values. Results are for the control dissipation case. The uncorrected analysis error is 130 m^2.

	Positive-dissipation SVs	Negative-dissipation SVs
Positive-dissipation singular values	381	510
Negative-dissipation singular values	195	255

TABLE 5. Corrected forecast error (m^2) based on the inexact forecast error using the full inverse composed of positive- or negative-dissipation SVs and singular values. Results are for the control dissipation case. The uncorrected analysis error is 245 m^2.

	Positive-dissipation SVs	Negative-dissipation SVs
Positive-dissipation singular values	148	230
Negative-dissipation singular values	110	120

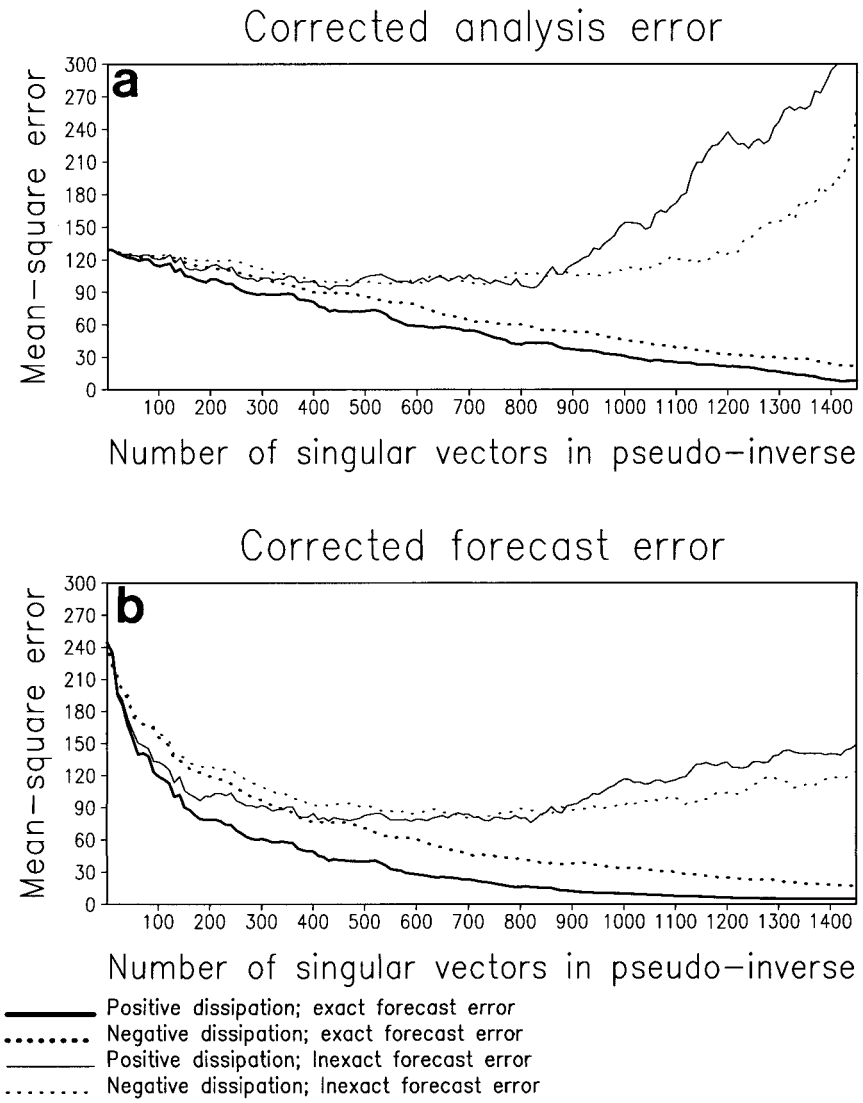

FIG. 6. (a) Corrected analysis error and (b) subsequent forecast error measured in global mean square geopotential height (m^2), as a function of the number of SVs included in the pseudoinverse. Positive-dissipation pseudoinverse denoted by solid curves. Negative-dissipation pseudoinverse denoted by dotted curves. Corrections based on the exact (inexact) forecast error denoted by thick (thin) curves.

ure 9 is the same as Fig. 8, except for strong dissipation. It is clear that the magnitude of the analysis error estimate is far too large to be realistic in the true-inverse case (Fig. 9a), but is close to the appropriate magnitude for the negative-dissipation backward integration (Fig. 9c). Comparing Fig. 9c to Fig. 7a shows that the analysis error estimate is reasonable over the Atlantic and over Europe and North Africa, but is poor in other regions, such as the North Pacific. This is because the backward integration of $\boldsymbol{\delta}$ (not shown) has a small amplitude over the Atlantic and Europe, and a large amplitude over the North Pacific, where it masks the true signal. Unfortunately, without the full spectrum of SVs, it is not possible to determine which part of the analysis error estimate to trust. The uncorrected mean square forecast error for the strong dissipation case (not shown) is 138 m^2. This is considerably smaller than the 245 m^2 for the control dissipation case (Fig. 7a), due to the damping effect of the strong dissipation on the forward-in-time growth of errors (Table 3). Because the signal (true forecast error) to noise (uncertainty in the verifying analysis) ratio is smaller in the strong dissipation case, the forecast error reductions are smaller, resulting in a near neutral impact for the true-inverse correction (142 m^2, Fig. 9b), and a 30% forecast error reduction for the negative-dissipation backward integration (97 m^2, Fig. 9d).

For comparison, the pseudoinverse initial perturbation and the adjoint-derived scaled sensitivity for the

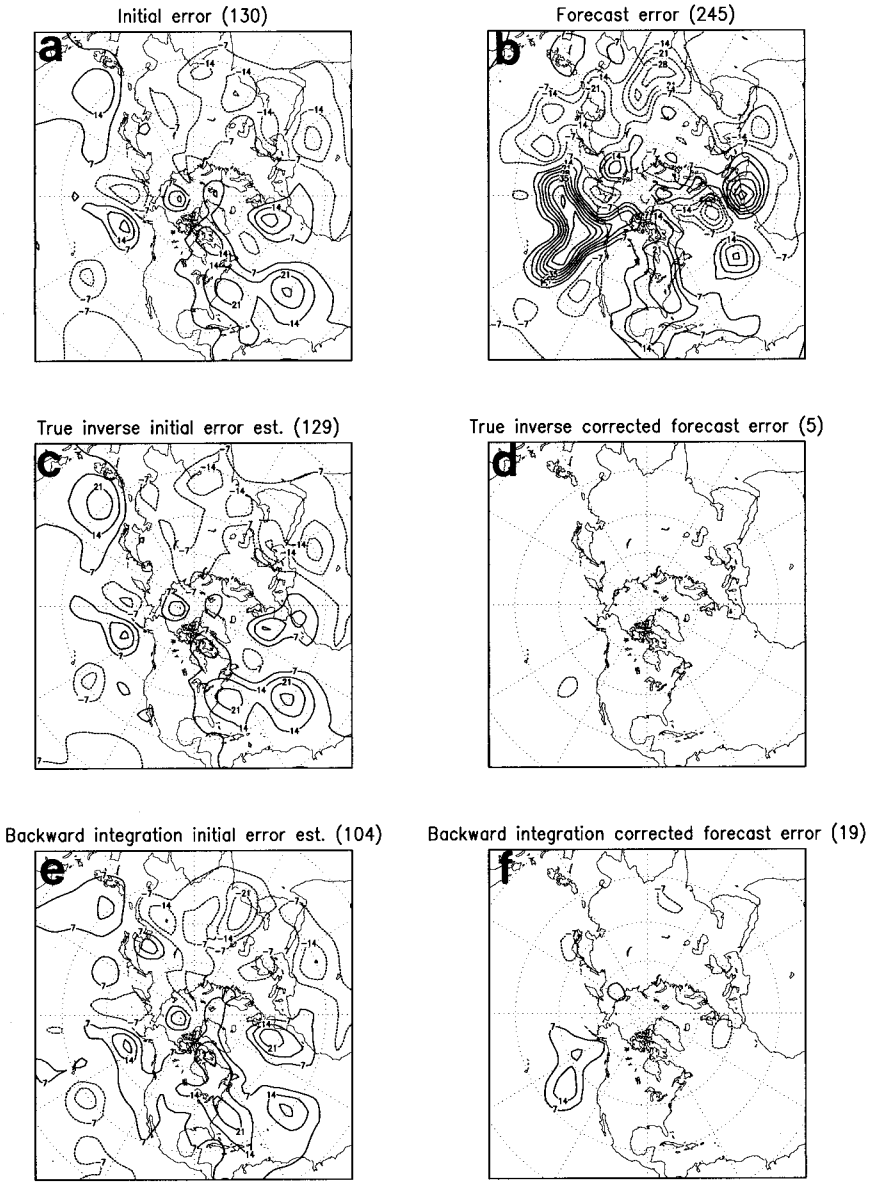

FIG. 7. The 500-mb geopotential height field associated with (a) the uncorrected initial analysis error $\mathbf{e}_a$; (b) the uncorrected forecast error $\mathbf{e}_f$; (c) the initial analysis error estimate using the positive-dissipation full inverse $\mathbf{e}_{a1}^{+}$ and (d) subsequent corrected forecast error $\mathbf{e}_{f1}^{+}$; and (e) the initial analysis error estimate using the negative-dissipation backward integration $\mathbf{e}_{a1}^{-\mathbf{B}}$ and (f) subsequent corrected forecast error $\mathbf{e}_{f1}^{-\mathbf{B}}$. The corrections are based on the exact forecast error and control dissipation. Contour interval is 7 m with the 0-m contour omitted. The mean square error (m^2) of each field is given in parentheses.

control dissipation case are also shown (Fig. 10). Note that the contour interval in Fig. 10 is 3.5 m^2 while the contour interval in Figs. 7–9 is 7 m^2. These perturbations are quite small (5–9 m^2) relative to the size of the full analysis error, but since they project strongly onto the growing part of that error, they result in large decreases in the forecast error (154–169 m^2 compared to 245 m^2). Note that: (i) these perturbations have similar spatial structures, (ii) they do not look like the full analysis error, and (iii) unlike the full-inverse or backward-integration perturbations, they are relatively insensitive to analysis uncertainty within the forecast error.

The impact of negative dissipation can also be examined in terms of energy spectra. Figure 11 shows the kinetic energy as a function of total wavenumber of the true initial analysis error (crosses) and the estimates of this error based on the positive-dissipation (clear circles) and negative-dissipation (solid circles) backward integrations. For the exact forecast error case (left panels), both estimates are reasonable, with both estimates too

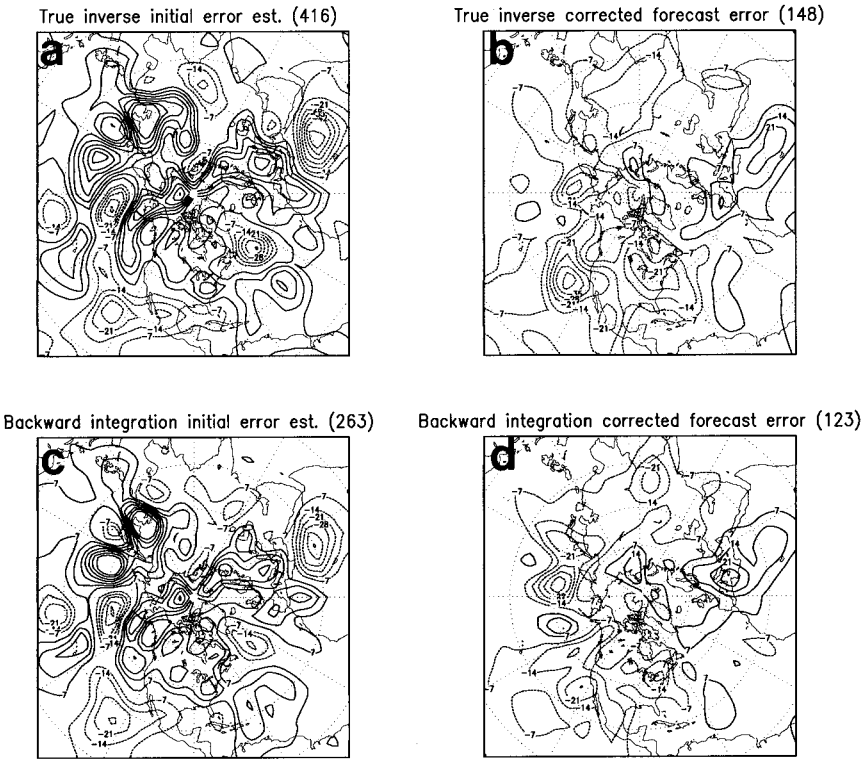

FIG. 8. The 500-mb geopotential height field associated with the (a) initial analysis error estimate using the positive-dissipation full inverse $\mathbf{e}_{a2}^{+}$ and (b) subsequent corrected forecast error $\mathbf{e}_{f2}^{+}$, and (c) initial analysis error estimate using the negative-dissipation backward integration $\mathbf{e}_{a2}^{-\mathbf{B}}$, and (d) subsequent corrected forecast error $\mathbf{e}_{f2}^{-\mathbf{B}}$. Corrections based on the inexact forecast error and control dissipation. Contour interval is 7 m and the 0-m contour interval is omitted. The mean square error (m^2) of each field is given in parentheses.

large at the 200-mb level, and the negative-dissipation estimate too small at the 800-mb level. For the inexact forecast error case (right panels), both estimates are far too large. However, the negative-dissipation estimate is smaller than the positive-dissipation estimate. The greatest impact of reversing the sign of the dissipation is seen at the 800-mb level at the highest wavenumbers. This is consistent with experiments that examine the impact of each of the three dissipation terms individually, which show that the 800-mb drag has the largest impact, followed by the horizontal scale-dependent diffusion. The Newtonian relaxation of temperature between levels has a minor impact.

To summarize the above results, for exact forecast errors, full-inverse and backward-integration methods give a good approximation of the full initial analysis error, even with negative dissipation. In contrast, the pseudoinverse method only estimates the fastest growing part of the initial analysis error. For inexact forecast errors, full-inverse and backward-integration methods do not result in a corrected analysis that is closer to the truth than the uncorrected analysis error, even when using strong negative dissipation. However, if the only goal is to find an analysis that results in an improved forecast, then full-inverse and backward-integration techniques can be quite effective.

These points can be further illustrated by examining the magnitude of the projection of the analysis error estimates onto the initial-time SVs. Figure 12a shows the projection of the true analysis error onto the initial-time SVs, $(\mathbf{e}_{a1}; \mathbf{u}_i^{+})$, as well as the projection of the true-inverse and negative-dissipation backward-integration estimates of the analysis error based on the exact forecast error, $(\mathbf{e}_{a1}^{+}; \mathbf{u}_i^{+})$ and $(\mathbf{e}_{a1}^{-\mathbf{B}}; \mathbf{u}_i^{+})$. The true-inverse method gives an analysis error estimate very close to the true analysis error (the thin solid line sits almost directly on top of the thick solid line). The negative-dissipation backward estimate is slightly less accurate, projecting too weakly onto the leading vectors and too strongly onto the trailing vectors (consistent with Fig. 3). These differences become more apparent for strong dissipation (not shown).

Figure 12b is the same as Fig. 12a except that the analysis error estimates are based on the inexact forecast error $(\mathbf{e}_f + \boldsymbol{\delta})$. The erroneous projection onto the decaying SVs is now clearly apparent, and is larger for the true inverse estimate than for the negative-dissipation backward integration estimate. Note that even

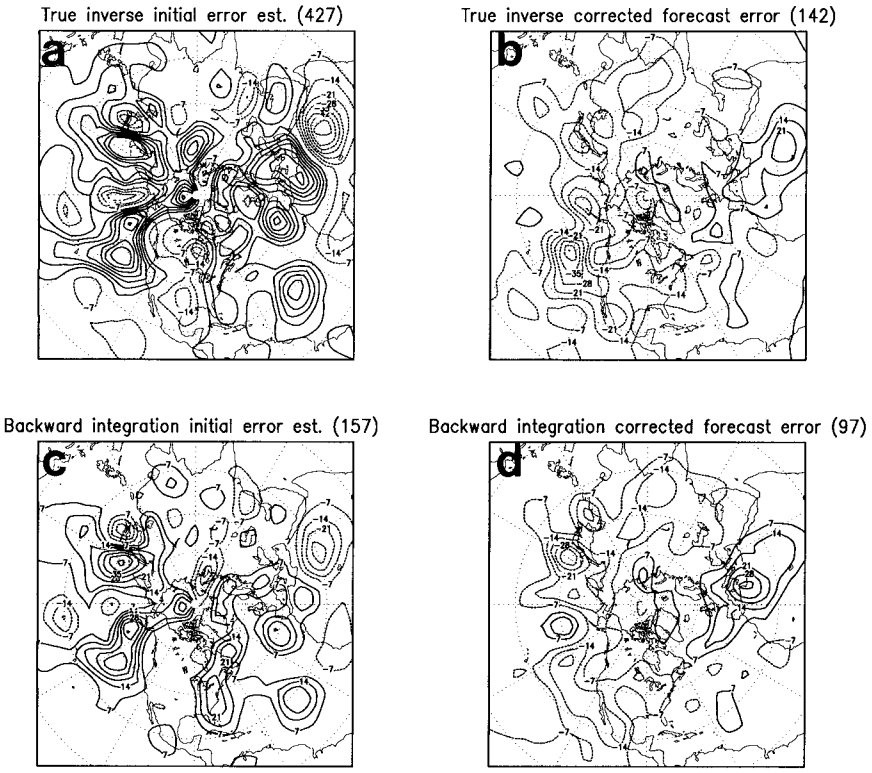

FIG. 9. Same as Fig. 8 but for strong dissipation.

though the erroneously large projection onto the decaying SVs is damped in the negative-dissipation case, the estimated analysis error is still dominated by the decaying SVs. This is also true for strong dissipation (not shown). In contrast, the perturbations produced by the pseudoinverse including only a few SVs (as well as adjoint-derived sensitivity, not shown) emphasize the growing modes and are thus relatively unaffected by the analysis uncertainty contained within the forecast error.

c. Regional correction techniques; implications for adaptive observations

All of the results presented so far have been for global error growth. There are many situations, such as for adaptive observations, when the region of interest is considerably smaller. Following Barkmeijer (1992) and Buizza (1994) a local projection operator is applied to the calculation of the SVs. This is done by finding the KE singular values not of $\mathbf{L}$, but of $\mathbf{PL}$, where the local projection operator $\mathbf{P} = \mathbf{S}^{-1}\mathbf{GS}$. Here, $\mathbf{S}$ is the matrix representation of the spectral-to-gridpoint transform, and $\mathbf{G}$ is a diagonal matrix, which masks out perturbations outside the region of interest. Note that the full inverse of $\mathbf{PL}$ does not exist, and that a number of the trailing singular values will be effectively zero, this number being a function of the size of the projection area. Applying this projection operator constrains the final-time SVs to optimize perturbation growth within the region of interest. The initial-time SVs may occur outside that region though. The local projection operator here corresponds to the Europe–western Asian region (referred to as the verification region) bounded by 30°W, 80°E, 30°N, and 80°N. An analogous technique is employed during the backward integration by first applying a mask to the forecast error field, which sets the field to zero outside the verification region, as described in Pu et al. (1998a,b).

Figure 13 shows the estimates of the initial perturbation that evolves into the forecast error within the verification region obtained using various methods. The mean-square geopotential height errors of the corrected forecasts over the verification region, along with the percent reductions from the uncorrected case, are indicated above each panel. The initial perturbation $\mathbf{e}_a$ is shown in Fig. 13a. The negative-dissipation backward integration applied to the exact forecast error produces an analysis perturbation, shown in Fig. 13c, that is very effective at reducing the forecast error over the verification region (the mean square forecast error is reduced from 259 m^2 to 50 m^2, a reduction of 81%). When the negative-dissipation backward integration is applied to the inexact forecast error (Fig. 13e), then the corrected forecast error is 113 m^2. This is still a significant reduction over the uncorrected forecast (56%). A comparison of Fig. 13c and Fig. 13e indicates a fair amount of sensitivity to the addition of uncertainty in the fore-

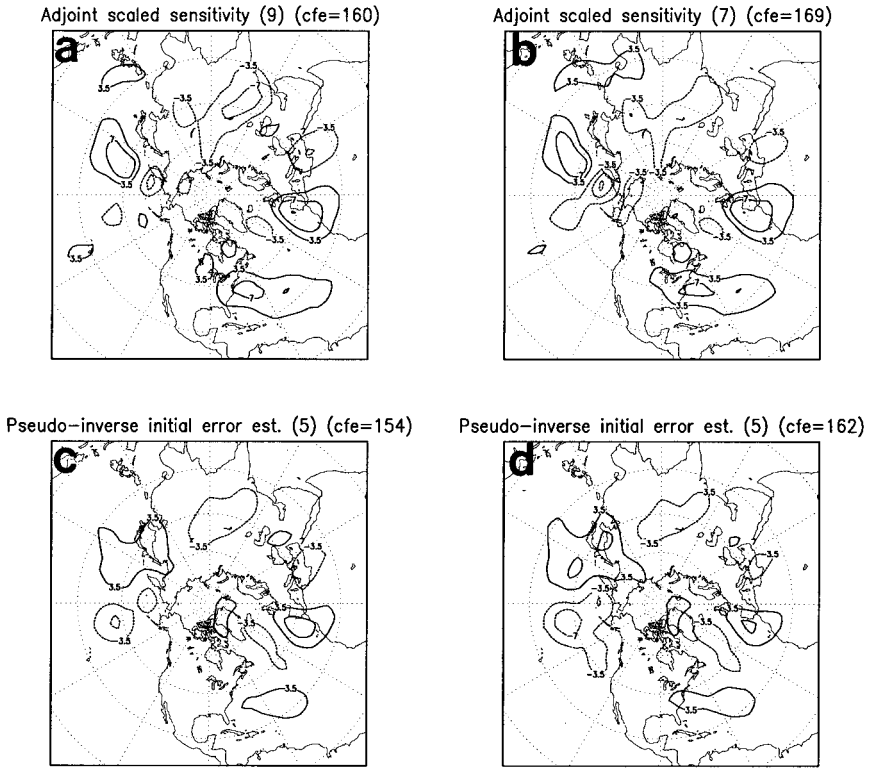

FIG. 10. The 500-mb geopotential height pattern associated with the adjoint-derived scaled sensitivity based on (a) the exact forecast error (i.e., $\mathbf{a}_{a1}$) and (b) the inexact forecast error (i.e., $\mathbf{a}_{a2}$). Analysis error estimate based on the pseudoinverse composed of the first 10 positive-dissipation singular vectors based on (c) the exact forecast error (i.e., $\mathbf{e}_{a1}^{+10}$) and (d) inexact forecast error (i.e., $\mathbf{e}_{a2}^{+10}$). Results shown are for the control dissipation case. Contour interval is 3.5 m with the 0-m contour omitted. The mean square error and corrected forecast error (m^2) of each field are given in parentheses.

cast error. The pseudoinverse corrections using the first 10 positive-dissipation SVs based on the exact (Fig. 13d) and inexact (Fig. 13f) forecast errors produce much smaller and more localized perturbations. As expected, they are relatively insensitive to the addition of uncertainty in the forecast error. The forecast error reductions produced by these much smaller perturbations over the verification region are 67% and 66% for the exact and inexact cases, respectively (a pseudoinverse composed of only the first three SVs results in a 50% reduction). These corrections are not as good as those obtained by using the much larger backward integration perturbation in the exact forecast error case (Fig. 13c), but better than those obtained by using the backward integration in the inexact forecast error case (Fig. 13e). The adjoint-derived scaled sensitivity (Fig. 13b) shows the expected similarity with the pseudoinverse perturbations (Figs. 13d,f).

A comparison of the backward integration and pseudoinverse perturbations suggests that the perturbations over western Asia present in Fig. 13c and absent in Fig. 13d represent a slowly growing or decaying part of the initial error. Inspection of the perturbations derived from pseudoinverse calculations using increasing numbers of SVs (not shown) confirms that most of the perturbation over western Asia does not appear until near neutral or decaying SVs are included in the pseudoinverse. (Only the first 50 SVs of **PL** are growing.)

Vertical cross sections (at 48°N) of the backward-integration and pseudoinverse estimates of the analysis error based on the exact forecast error are shown in Fig. 14. They correspond to the fields shown in Figs. 13c,d, respectively. Consistent with results in several previous studies (e.g., Molteni and Palmer 1993), the pseudoinverse estimate (Fig. 14b) has a westward tilt with height and a maximum amplitude at 500 mb. In contrast, the backward-integration estimate (Fig. 14a) has a maximum amplitude at 200 mb. To the west of the Greenwich meridian this perturbation has a slight westward tilt with height, characteristic of growing perturbations, while to the east of the meridian this perturbation has a slight eastward tilt with height, characteristic of decaying perturbations (RP98). Setting the analysis error to zero in the eastern and western regions confirms the relative impact of the regional analysis errors on the forecast error. Setting the analysis error to zero in the region south of Greenland (37°–57°N, 50°–28°W), centered on the maximum in the backward-integration estimate (Fig.

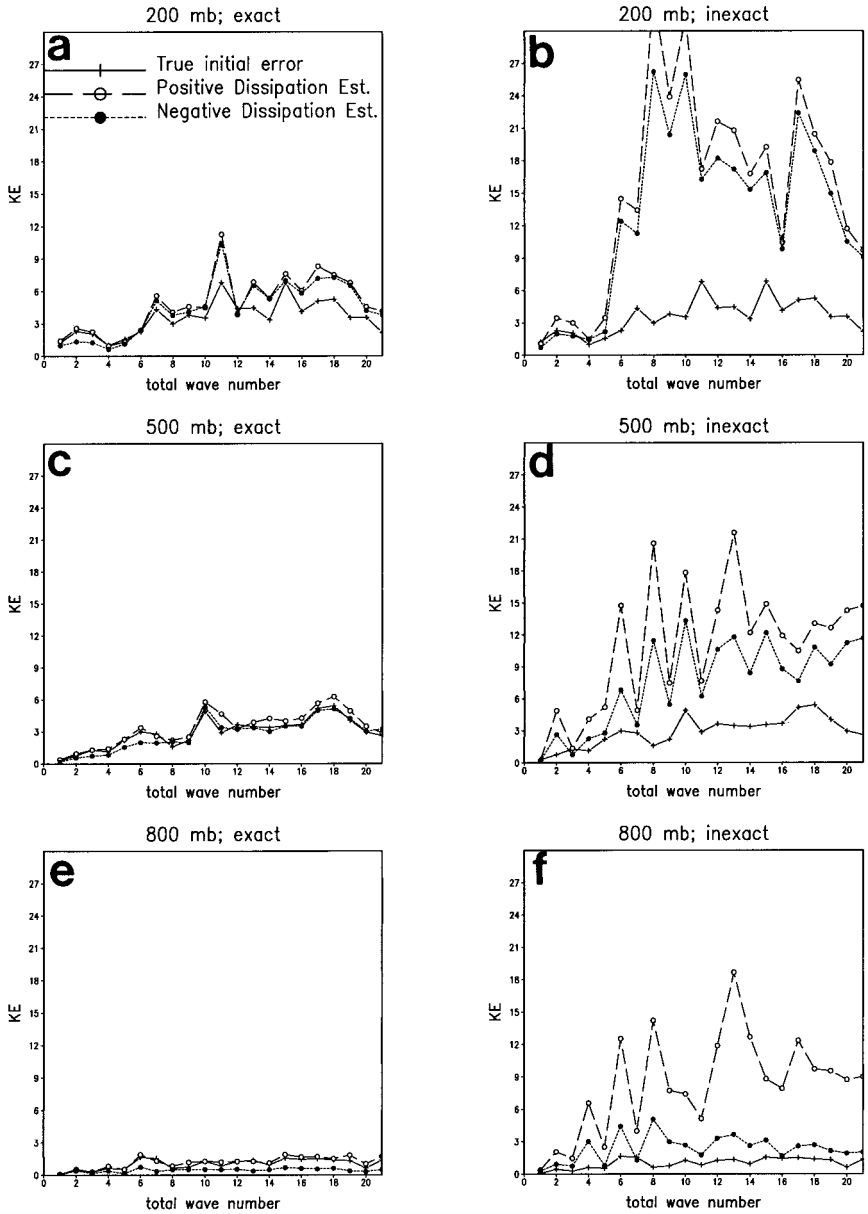

FIG. 11. The kinetic energy ($m^2\ s^{-2}$) as a function of total wavenumber for the true initial analysis error (denoted by crosses), and the estimates of the initial analysis error given by the positive-dissipation backward integration (clear circles) and the negative-dissipation backward integration (solid circles). The estimates based on the exact forecast error are given in (a), (c), and (e) for the 200-, 500-, and 800-mb levels, respectively. The estimates based on the inexact forecast error are given in (b), (d), and (f), for the 200-, 500-, and 800-mb levels, respectively.

13c), results in a forecast error reduction of 34%. Setting the analysis error to zero in the region west of Spain (31°–53°N, 28°–6°W), centered on the maximum in the pseudoinverse estimate (Fig. 13d), results in a 44% forecast error reduction. In contrast, setting the analysis error to zero over western Asia (25°–82°N, 28°–79°E, also corresponding to local maxima in Fig. 13c) had almost no impact (a 2% reduction) on the forecast error. Examination of the projection of the initial perturbations onto the initial-time SVs (not shown) confirms that, as designed, the pseudoinverse perturbation and adjoint-derived sensitivity are dominated by the fast-growing SVs. In contrast, the full inverse and backward integration perturbations project fairly equally onto the growing and decaying modes in the exact forecast error case.

It should be noted that there are significant differences between these experiments and techniques that could be

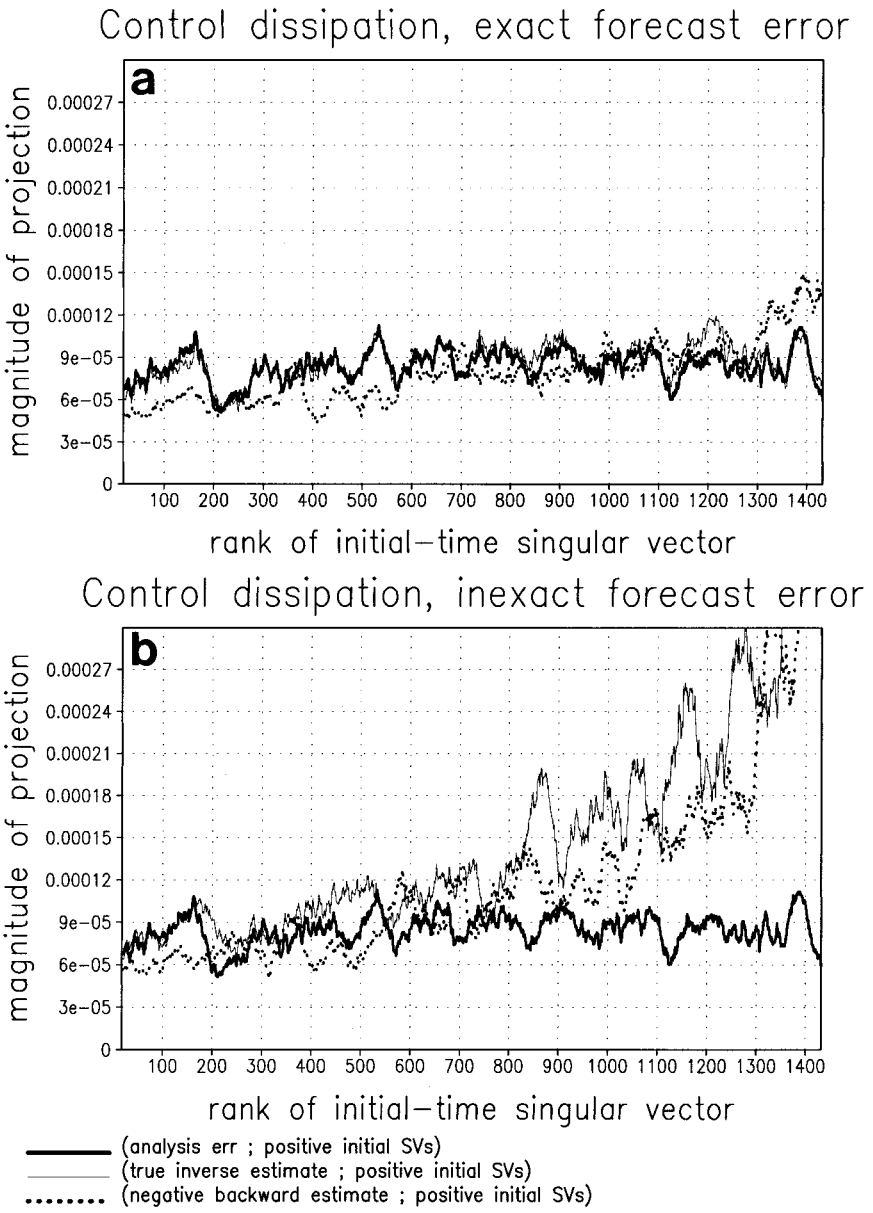

FIG. 12. The magnitude of the projection of the analysis error (thick solid), positive-dissipation full-inverse estimate of the analysis error (thin solid), and negative-dissipation backward-integration estimate of the analysis error (dotted) onto the positive initial-time SVs as a function of rank for the control dissipation case. The corrections are based on the (a) exact forecast error and (b) inexact forecast error.

used for adaptive observations in practice. These experiments are based on forecast errors, obviously not available in real time. Substituting forecast differences, such as between ensemble members (as in Pu et al. 1998a,b), for the true forecast error may have a significant impact on the results. Likewise, using SVs themselves, rather than the pseudoinverse operating on the forecast error, will be useful only if the true analysis error has a sufficiently large projection onto the leading SVs. Current experiments are being conducted in a manner that is more consistent with operational constraints in order to explore implications for adaptive observations more thoroughly.

6. Summary and conclusions

The method of running the tangent equations with a negative time step to approximate the full inverse of the forward tangent propagator (Pu et al. 1997; Wang et al. 1997) was shown to be a good approximation of the

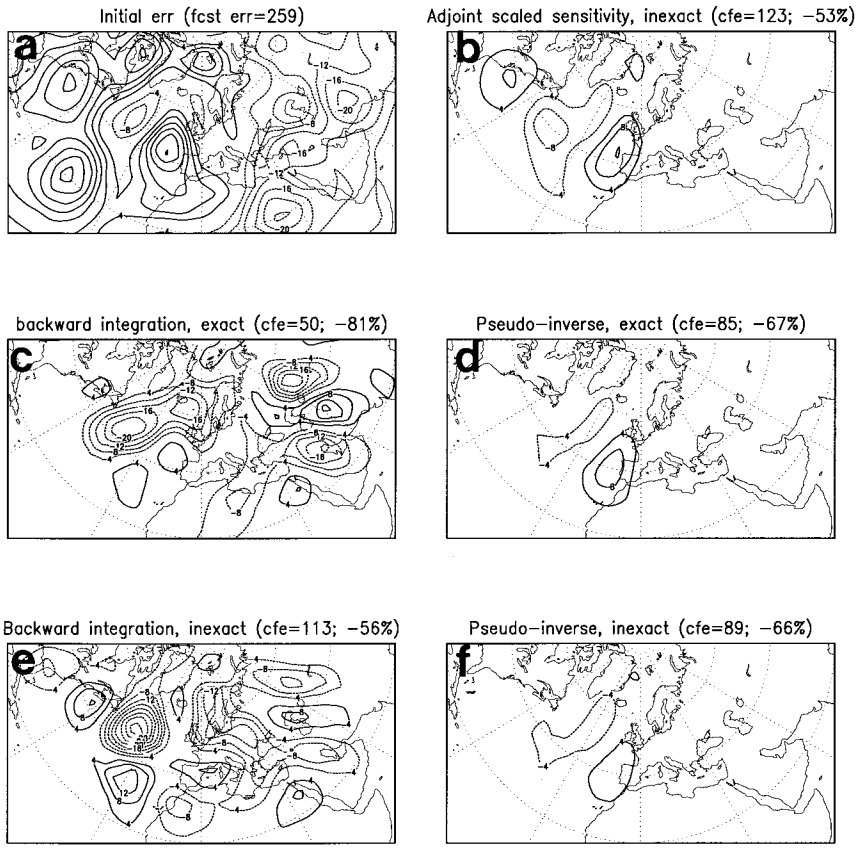

FIG. 13. The 500-mb geopotential height field associated with (a) the analysis error $\mathbf{e}_a$ and (b) the adjoint-derived scaled sensitivity based on the inexact forecast error. The initial-time perturbation based on the negative-dissipation backward integration based on the (c) exact and (e) inexact forecast error. The initial-time perturbation based on the pseudoinverse composed of the first 10 positive-dissipation SVs based on the (d) exact and (f) inexact forecast error. Results shown are for the control-dissipation case. Contour interval of 4 m with 0-m contour omitted. The subsequent mean square forecast errors (m^2) and percent reduction from the uncorrected forecast error over the verification region are shown above each panel.

true inverse in a simple quasigeostrophic model in RP98. RP98 was also able to show that although true-inverse and backward-integration techniques provide very good estimates of the initial analysis error when based on exact forecast errors, they produce unrealistically large approximations of the initial analysis error when uncertainty is present in the forecast error, owing to the erroneous projection of this uncertainty onto the final-time trailing SVs. RP98 also found that reversing the sign of the dissipation during the backward integration [done in Pu et al. (1997) for computational stability] significantly damps this backward growth of uncertainty. It is the nature of this damping effect that is investigated in detail in this study.

The negative-dissipation backward integration is found to be a very good approximation to the exact inverse of the forward tangent propagator computed with negative dissipation (Table 2). This allows for an investigation of the impact of the sign of the dissipation through negative-dissipation singular values and SVs. Even though the structures of the SVs change with negative dissipation (Fig. 2), the analysis and forecast corrections based on exact forecast errors are still quite good (the estimate of the analysis error becomes slightly biased toward the trailing SVs, Fig. 12a). For inexact forecast errors, the analysis uncertainties are just as likely to project onto the negative-dissipation trailing SVs as onto the positive-dissipation trailing SVs (Fig. 4). Therefore the damping effect on the backward growth of noise observed when using negative dissipation (Fig. 6) is due to the fairly uniform change in the singular values, not due to a structural change in the SVs. The estimate of the analysis error is smaller when using negative dissipation, but it is still dominated by the decaying SVs (Fig. 12b). This may not be disadvantageous if the only goal is to produce an improved forecast, regardless of the size of the initial perturbation, but it is disadvantageous if one is looking for the fastest growing part of the analysis error.

The differences between the full-inverse or backward-

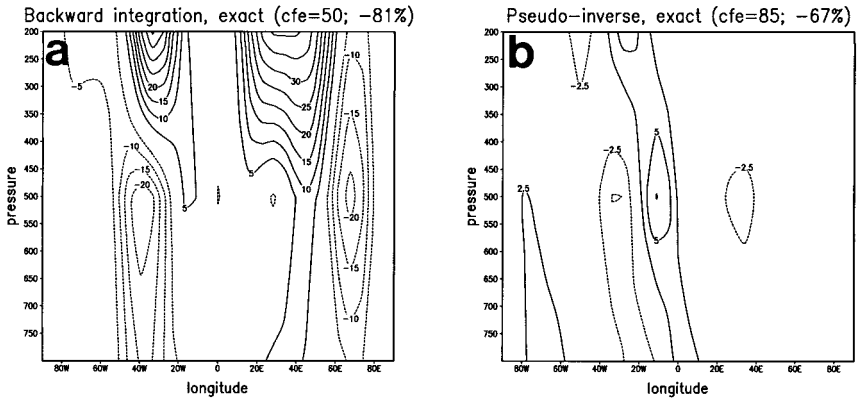

FIG. 14. A vertical cross section at 48°N of the geopotential height field associated with the initial-time perturbation based on (a) the negative-dissipation backward integration and (b) the pseudoinverse composed of the first 10 positive-dissipation SVs, based on the exact forecast error for the control dissipation case. Contour interval of (a) 5 m and (b) 2.5 m with 0-m contour omitted. The subsequent mean square forecast errors and percent reduction from the uncorrected forecast error over the verification region are shown above each panel.

integration perturbations and the pseudoinverse perturbations when using a local projection operator are also significant (Fig. 13). The former finds the full initial perturbation that evolves into the forecast error over the verification region, while the latter finds only the fastest growing part. Changing the sign of the dissipation does not alter this result. To use the full-inverse or backward-integration results for adaptive observations, one would need to find a way to distinguish between the growing and decaying parts of the signal. Pu et al. (1998b) also note differences between the adjoint and backward-integration methods and suggest using a combination of both methods for adaptive observations.

There are some specific conditions under which one might expect a full-inverse or backward-integration technique based on an exact forecast error to produce a perturbation that is collocated with the adjoint sensitivity or pseudoinverse perturbations. If the initial difference between the two forecasts is composed primarily of the growing part of the spectrum (as opposed to the fairly isotropic initial analysis error shown in Fig. 3), then the estimate of this error will likewise be dominated by the growing part of the spectrum. Targets would also be similar if the largest initial error is also very fast growing. Also, it is quite possible that the growing and decaying components of the initial error may be horizontally collocated (results not shown indicate that the leading and trailing SVs often come in collocated pairs), especially if the verification region is small. However, even if the perturbations are horizontally collocated, the vertical structures should still be quite different (Fig. 14; Pu et al. 1998b). This may be immaterial if the desired output is dropwindsonde location (and the dropwindsondes can be dropped from a sufficiently high altitude) but important if the target region needs to be specified in the vertical as well as the horizontal.

There are several limitations of this study, primarily owing to its simplicity, that must be considered when drawing conclusions from the results. This study is conducted under the perfect-model assumption. No consideration has been given to model errors, which could have a significant impact. Ménard and Daley (1996) find that applying a 4D variational algorithm (using a perfect-model assumption) when the model is imperfect, may result in larger errors, especially at the beginning and end of the assimilation period. Also, the forward tangent propagator used here is based on the exact tangent equations of the nonlinear model. In complex forecast models, simplifications in the moist physics are often made in the tangent and adjoint equations. [Ehrendorfer and Errico (1995) have shown significant differences between dry and moist SVs.] The corrections obtained should degrade as the forward tangent propagator becomes a worse approximation to the nonlinear forecast model and the real atmosphere.

Another simplification is that only analysis differences, not real analysis errors, are used in this study. It is impossible at this time to determine whether analysis errors are approximately isotropic with respect to the initial-time SVs, although there is indirect evidence that this assumption is true for the first 30 total energy SVs (Gelaro et al. 1998). To examine the robustness of these results to uncertainties in the characteristics of the analysis errors, different types of random perturbations are also considered as $\boldsymbol{\delta}$. Random perturbations are constructed to have a peak in KE at either small, medium, or large spatial scales, where the medium scale perturbations also have more energy at the 200- and 500-mb levels than the 800-mb level. [Daley and Mayer (1986) use an observation system simulation experiment to produce an estimate of analysis error that has a KE spectral peak at around wavenumber 10, and more energy at mid- and upper-tropospheric levels than at the lower-tropospheric levels.] Five cases are considered for each

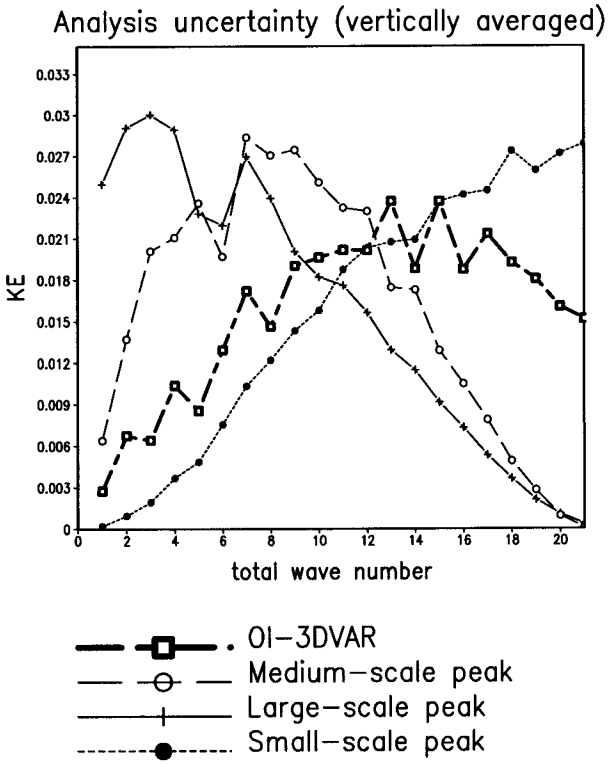

FIG. 15. The kinetic energy ($m^2\ s^{-2}$) as a function of total wavenumber for the OI–3DVAR estimate of $\boldsymbol{\delta}$ (clear squares), small-scale $\boldsymbol{\delta}$ (solid circles), medium-scale $\boldsymbol{\delta}$ (clear circles), and large-scale $\boldsymbol{\delta}$ (crosses).

configuration and their average KE spectra, compared with the OI–3DVAR spectra, are shown in Fig. 15 (the perturbations have been normalized to have a total KE of 1). Table 6 gives the linear growth of perturbation variance during the inverse calculation (i.e., $\Sigma_{i=1}^{1449}[(\boldsymbol{\delta};\mathbf{v}_i)/\sigma_i]^2$) for the different types of perturbations. The five-case mean is the first number, and the range is given in parentheses. The medium-scale perturbation growth is similar to that for OI–3DVAR. On the other hand, the large- and small-scale perturbation growth is smaller (the perturbations would actually decay for the strong-dissipation case). Experiments using these small-scale or large-scale random perturbations for $\boldsymbol{\delta}$ (scaled to an appropriate magnitude) show smaller error growth during the backward integration, resulting in a near neutral impact on the initial analysis error in most cases, and a 16% and 24% reduction in the initial analysis error in the best control- and strong-dissipation cases found. The growth of noise in the backward direction may therefore be overestimated should the true analysis errors have smaller projections onto the final-time trailing SVs than the OI–3DVAR differences.

Singular values and SVs are metric dependent (full-inverse and backward-integration calculations are not). Only results based on a KE metric have been shown here. However, results based on a streamfunction-squared metric (not shown) lead to the same conclusions. The results presented here are for three cases only (control, medium, and strong dissipation), but six other cases examined give similar results. Also, only results for 48-h optimization time have been shown. Similar experiments were carried out for optimization times of 12, 24, and 72 h, yielding qualitatively similar results. The growth of uncertainty in the backward integration (and therefore the corrected analysis error) is smaller for shorter optimization times. The corrected analysis error based on the negative-dissipation backward integration of the inexact forecast error is 142 m^2 for the 12-h case compared to 261 m^2 for the 48-h case (still larger than the initial analysis error of 130 m^2). Also, the impact of reversing the sign of the dissipation is smaller for shorter optimization times, but is still significant for the 12-h case. Unfortunately, the percent reduction in forecast error is also smaller for the 12-h and 24-h cases (i.e., 3% and 17%, respectively) than for the 48-h case (48%). This is because the signal (forecast error) to noise (analysis uncertainty) ratio is much smaller for the shorter optimization times.

TABLE 6. The linear growth of the variance of uncertainty during the inverse operation (i.e., $\sum_{i=1}^{1449}[(\boldsymbol{\delta};\mathbf{v}_i)/\sigma_i]^2$). The five-case mean is given first, with the range given in parentheses.

	Control dissipation	Strong dissipation
OI-3DVAR	1.96 (1.79–2.20)	1.13 (1.07–1.24)
Medium-scale peak	1.81 (1.68–1.91)	1.12 (1.05–1.26)
Large-scale peak	1.59 (1.46–1.66)	0.91 (0.87–0.94)
Small-scale peak	1.13 (1.04–1.23)	0.71 (0.66–0.75)

For the simple model used here, $\mathbf{L}$ is nonsingular (invertible). For complex operational models, $\mathbf{L}$ may be singular, and the size of the null-space may be a function of the dissipation. Experiments should be carried out to assess the sensitivity of inverse-type methods to dissipation strength in operational models, perhaps in a perfect-model context with prescribed initial perturbations. Similar experiments may be useful in obtaining an estimate of the statistical properties of the decaying SVs (which cannot be calculated explicitly for large systems), which may contaminate backward-integration estimates of analysis error.

Despite these limitations, we believe the conclusions drawn from these results should be applicable to more complex systems. The decision as to which type of technique to use should be based on a full consideration of the advantages and drawbacks of each method, some of which are reiterated here. The pseudoinverse technique, like adjoint sensitivity, is designed to find only the fastest growing part of the analysis error and is relatively insensitive to the analysis uncertainty contained within the forecast error. This makes these methods well suited for adaptive observations. On the other hand, the full-inverse and backward-integration methods are designed to find the entire analysis error but are much more sensitive to the backward growth of uncertainty in the fore-

cast error. This is true even if negative dissipation is used in the backward integration, and if the inverse is applied only to a localized region of the forecast error. Nonetheless, since this analysis error estimate is dominated by decaying perturbations, the subsequent corrected forecast errors are as good as, or better than, those derived by pseudoinverse techniques. If the desired product is an analysis perturbation that will produce a significantly corrected forecast, not an analysis that is closer to the truth, then relatively inexpensive full-inverse techniques can be very useful.

Acknowledgments. The author would like to thank Ron Errico, Ron Gelaro, and Tim Palmer for helpful discussions. Tim Palmer suggested the analysis perturbation experiments discussed in the last part of section 5b. The three-level quasigeostrophic model was developed by Franco Molteni. Support of the sponsor, Office of Naval Research, and the program manager, Naval Research Laboratory, Project Element 0601153N, is gratefully acknowledged. Computing support was provided by the DoD High Performance Computing program.

REFERENCES

Andersson, E., P. Courtier, W. Heckley, F. Rabier, J. N. Thépau, P. Undén, and D. Vasiljevic, 1995: Pre-operational tests with a three-dimensional variational analysis scheme. *Proc. WMO Second Int. Symp. on Assimilation of Observations in Meteorology and Oceanography,* Tokyo, Japan, WMO, 43–48.

Barkmeijer, J., 1992: Local error growth in a barotropic model. *Tellus,* **44A,** 314–323.

——, P. Houtekamer, and X. Wang, 1993: Validation of a skill prediction method. *Tellus,* **45A,** 424–434.

——, M. van Gijzen, and F. Bouttier, 1998: Singular vectors and the analysis error covariance metric. *Quart. J. Roy. Meteor. Soc.,* **124,** 1695–1714.

Buizza, R., 1994: Localization of optimal perturbations using a projection operator. *Quart. J. Roy. Meteor. Soc.,* **120,** 1647–1681.

——, 1998: Impact of horizontal diffusion on T21, T42, and T63 singular vectors. *J. Atmos. Sci.,* **55,** 1069–1083.

——, R. Gelaro, F. Molteni, and T. N. Palmer, 1997: The impact of increased resolution on predictability studies with singular vectors. *Quart. J. Roy. Meteor. Soc.,* **123,** 1007–1033.

Cohn, S. E., N. S. Sivakumaran, and R. Toding, 1994: A fixed-lag Kalman smoother for retrospective data assimilation. *Mon. Wea. Rev.,* **122,** 2838–2867.

Daley, R., and T. Mayer, 1986: Estimates of global analysis error from the Global Weather Experiment Observational Network. *Mon. Wea. Rev.,* **114,** 1642–1653.

Ehrendorfer, M., and R. M. Errico, 1995: Mesoscale predictability and the spectrum of optimal perturbations. *J. Atmos. Sci.,* **52,** 3475–3500.

——, and J. J. Tribbia, 1997: Optimal prediction of forecast difference covariances through singular vectors. *J. Atmos. Sci.,* **54,** 286–313.

Farrell, B., 1990: Small error dynamics and the predictability of atmospheric flows. *J. Atmos. Sci.,* **47,** 2409–2416.

Gelaro, R., E. Klinker, and F. Rabier, 1996: Real and near-real time corrections to forecast initial conditions using adjoint methods: A feasibility study. Preprints, *11th Conf. on Numerical Weather Prediction,* Norfolk, VA, Amer. Meteor. Soc., J58–J60.

——, R. Buizza, T. N. Palmer, and E. Klinker, 1998: Sensitivity analysis of forecast errors and the construction of optimal perturbations using singular vectors. *J. Atmos. Sci.,* **55,** 1012–1037.

Lorenz, E. N., 1965: A study of the predictability of a 28-variable atmospheric model. *Tellus,* **17,** 321–333.

Marshall, J., and F. Molteni, 1993: Toward a dynamical understanding of planetary-scale flow regimes. *J. Atmos. Sci.,* **50,** 1792–1818.

Ménard, R., and R. Daley, 1996: The application of Kalman smoother theory to the estimation of 4DVAR error statistics. *Tellus,* **48A,** 221–237.

Molteni, F., and T. N. Palmer, 1993: Predictability and finite-time instability of the northern winter circulation. *Quart. J. Roy. Meteor. Soc.,* **119,** 269–298.

Mureau, R., F. Molteni, and T. N. Palmer, 1993: Ensemble prediction using dynamically conditioned perturbations. *Quart. J. Roy. Meteor. Soc.,* **119,** 299–323.

Palmer, T. N., R. Gelaro, J. Barkmeijer, and R. Buizza, 1998: Singular vectors, metrics and adaptive observations. *J. Atmos. Sci.,* **55,** 633–653.

Pires, C., R. Vautard, and O. Talagrand, 1996: On extending the limits of variational assimilation in nonlinear chaotic systems. *Tellus,* **48A,** 96–121.

Pu, Z.-X., E. Kalnay, J. Sela, and I. Szunyogh, 1997: Sensitivity of forecast errors to initial conditions with a quasi-inverse linear method. *Mon. Wea. Rev.,* **125,** 2479–2503.

——, E. Kalnay, and Z. Toth, 1998a: Application of the quasi-inverse linear and adjoint NCEP global models to targeted observations during FASTEX. *Proc. 12th Conf. Numerical Weather Prediction,* Phoenix, AZ, Amer. Meteor. Soc., 8–9.

——, S. Lord, and E. Kalnay, 1998b: Forecast sensitivity with dropwindsonde data and targeted observations. *Tellus,* **50A,** 391–410.

Rabier, F., E. Klinker, P. Courtier, and A. Hollingsworth, 1996: Sensitivity of forecast errors to initial conditions. *Quart. J. Roy. Meteor. Soc.,* **122,** 121–150.

Reynolds, C. A., and T. N. Palmer, 1998: The impact of decaying singular vectors on analysis and forecast correction. *J. Atmos. Sci.,* **55,** 3005–3023.

Wang, Z, K. K. Droegemeier, L. White, and I. M. Navon, 1997: Application of a new adjoint newton algorithm to the 3D ARPS storm-scale model using simulated data. *Mon. Wea. Rev.,* **125,** 2460–2478.